Advanced Decoration of Cost-Effective Transitional Metals for Photocatalytic Hydrogen Production

Shadrack Yimbila

A Thesis
In
the Department
of
Chemical and Materials Engineering

Presented in Partial Fulfillment of the Requirements
For the Degree of Master of Applied Science at
Concordia University
Montreal, Quebec, Canada

August 2024

Concordia University

School of Graduate Studies

This is to certify that the thesis prepared

By: Shadrack Yimbila

Entitled: Advanced Decoration of Cost-Effective Transitional Metals for Photocatalytic Hydrogen Production

and submitted in partial fulfillment of the requirements for the degree of

Master of Applied Science (Chemical Engineering)

complies with the university's regulations and meets the accepted standards concerning originality and quality.

Signed by the final Examining Committee:

_____ Chair

Dr. Yaser Khojasteh

_____ Examiner

Dr. Ivan Kantor

_____ Supervisor

Dr. Nhat Truong Nguyen

Approved by _____

Dr. Zhibin Ye, Graduate Program Director

` August 2024 _____

Dr. Mourad Debbabi, Dean Gina Cody School of Engineering and Computer Science

ABSTRACT

Advanced Decoration of Cost-Effective Transitional Metals for Photocatalytic Hydrogen Production

Shadrack Yimbila

Throughout history, the energy crisis has predominantly arisen from inadequate supply rather than depletion of resources. From the utilization of fire to the development of steam engines and, subsequently, the utilization of fossil fuels and renewable energy sources, humanity has consistently adapted to meet its energy needs. Particularly noteworthy, hydrogen stands as a significant and renewable energy source. However, the demand for hydrogen has tripled since 1975, and due to technological limitations and high costs, most of its production still depends on fossil fuels. Various approaches have been employed to address this issue, one of which is photocatalysis, which holds promise in mitigating the adverse effects of fossil fuel production. Nevertheless, this method has limitations regarding light absorption and the recombination of charged particles. Zero and one-dimensional nanostructures, such as nanotubes, have been extensively investigated as potential photocatalysts, as they exhibit unique properties, including a high aspect ratio that facilitates the controlled movement of charges in a single direction. In order to overcome the aforementioned limitations, modifications have been made to these nanostructures.

However, conventional methods employed for these modifications have drawbacks, such as the extensive use of toxic solvents, limited control over the process, time constraints, and lack of reproducibility. In contrast, greener synthesis methods, such as microwave deposition and liquid-assisted resonant acoustic mixing (LA-RAM), have emerged as viable alternatives due to their minimal energy input and reduced reliance on toxic solvents. Moreover, microwave deposition and liquid-assisted resonant acoustic mixing offer advantages such as shorter reaction times, controlled and uniform deposition, scalability, and improved reproducibility, which address the challenges faced by conventional methods. In this study, transitional metals, namely copper and nickel, were decorated onto titania nanoparticles using LA-RAM and titanium nanotubes using microwave deposition. The individual and combined effects of copper and nickel decoration were investigated alongside optimizing some reaction parameters. Compared to conventional noble metal decoration and traditional synthesis, the photocatalytic efficiency of the resulting best outcome proved to be a practical and effective option. This research is a foundation for further exploration and utilization of greener and more cost-effective methods and metals in synthesizing photocatalysts.

ACKNOWLEDGEMENT

First, I would like to thank God almighty for the gift of life and strength throughout this journey. My heartfelt appreciation goes to my supervisor, Dr. Nhat Truong Nguyen, for his invaluable support, patience, and guidance throughout this journey. I am thankful for the opportunities and trust you gave me, which helped me grow as a researcher in this field.

Again, I express my sincere gratitude to Dr. Marek Majewski(Chemistry Dept) for granting me access to his lab for this project. Special thanks to Camilo Viasus (McGill) for collaborating on the LA-RAM and XPS characterization of the samples. My uttermost appreciation also goes to Camilo Perdomo and Joseph Daniel Chiong for their various roles and valuable contributions to this project. Moreover, I am also grateful to Harriet Laryea for her enormous support during this journey.

Furthermore, I am eternally grateful to my family, particularly my parents, Mr. and Mrs. Yimbila, whose personal sacrifices, counsel, and prayers have been the cornerstone of my development and success.

In addition, I am deeply indebted to the Church of Pentecost, West Island Assembly, for the spiritual support and the wonderful family I have found in them. Your prayers, love, and encouragement have been a source of comfort and inspiration and deeply touched my heart, keeping my soul stilled throughout this journey.

Finally, to the entire department, all who have contributed directly or indirectly, I am very grateful for your support.

Contents

TABLE OF FIGURES

LIST OF TABLES

ABBREVIATION

SRM Steam Methane Reforming
CG Coal Gasification
LCOH Levelized Cost of Hydrogen
PV-EC Photovoltaic Electrochemical system
AP Acidification Potential
GP Global warming potential
PEC Photoelectrochemical system
STH Solar to Hydrogen efficiency
PC Photocatalysis
PC I Photocatalyst I
PC II Photocatalyst II
PB Photobiolysis
PV Photovoltaic
CCS Carbon Capture System
BoS Balance of System
UV Ultraviolet
CB Conduction Band
VB Valence Band
SPR Surface Plasmon Resonance
OP Oxidation Photocatalyst
RP Reduction Photocatalyst
CNT Carbon nanotube
HER Hydrogen Evolution Reaction
OER Oxygen Evolution Reaction
TEOA Triethanolamine
SEM Scanning Electron Microscope
EDS Energy Dispersive Spectroscopy
XRD X-Ray Diffraction
HR-TEM High-Resolution Transmission Electron Microscope
ICP-MS Inductively Coupled Plasma Mass Spectroscopy

CHAPTER 1: BACKGROUND INFORMATION

Globalization and industrialization have contributed to the increased need for energy. Most energy is produced from fossil fuels, accounting for approximately 80% of global energy production [1]. Despite their critical role in meeting global energy demands, they contribute three-fourths of greenhouse gas emissions. CO_2, a significant greenhouse gas, is the leading contributor to global warming. In 2020 alone, fossil fuels generated 34.8 billion metric tons of CO_2 [2]. Aside from the negative environmental impact, the continuous exploitation of these sources poses a grave threat to energy security in the foreseeable future due to the ever-increasing population. The finite nature and its environmental issues have led to a need for renewable and sustainable energy sources to replace these dominant conventional ones. Several renewable sources, like solar, tidal, wind, and so on, have been investigated and applied in diverse areas. However, they have failed to replace conventional sources with fossil fuels because of problems such as intermittency, storage challenges, and a costly initial setup [3,4].

Hydrogen, a feasible energy carrier, shows promise in this shift towards clean and sustainable energy. After the oil crisis in 1970, hydrogen emerged as a fuel for energy systems. Nevertheless, it garnered much interest and attention after the invention of fuel cell technology in 1990 [4]. The reason for this interest is its high energy capacity, and unlike fossil fuels, the byproduct of hydrogen combustion is merely water [5]. It is also easy to store and transport in pipes, which is a limitation of some renewable sources. Although most of it is currently generated from fossil fuels, it may also be produced from water, biomass, and the sun, which are abundant and eternal sources [3].

Several green hydrogen production methods have been researched; however, photocatalytic water splitting is one promising process because of its feedstock's abundant and perpetual nature: water and sun [6]. Photocatalysis is the generation of charge carriers from a semiconductor after irradiation to undergo a redox reaction. The main constraints of this process are the restricted absorption spectrum and the fast recombination of charge carriers. Several approaches, such as doping and decorating photocatalysts, have been applied to boost efficiency [7]. Since Honda and Fujishima's revolutionary use of TiO_2 nanoparticles to split water, titanium dioxide has been mostly used owing to its low cost, chemical stability, and environmental friendliness [8]. Various morphologies of TiO_2 have been examined with adjustments to optimize its absorption spectrum and increase the lifetime of charge carriers [7]. Furthermore, numerous synthetic methods, such as the sol-gel method, coprecipitation, hydrothermal, and ball milling, have been explored to produce photocatalysts [9]. However, the significant issue with some of these conventional methods is the extensive use of solvents and energy.

Currently, most noble metals have been used as cocatalysts due to their high work function and ability to catalyze hydrogen evolution reactions (HER). However, these noble metals' expensive and limited nature has led to the exploration of earth-abundant and cost-effective transitional metals such as Cu and Ni. These metals have been found to have a high work function and catalyze hydrogen evolution reaction (HER). They can form a Schottky barrier with the photocatalyst, which helps spatially separate charge carriers and prevents back reaction of the hydrogen and oxygen. Copper, for instance, also exhibits a surface plasmon effect, which helps in improving light absorption in the visible range [10-13].

In this project, the microwave-assisted decoration of titania nanotubes was examined, and liquid-assisted resonant acoustic mixing was also used to decorate titania nanoparticles. The decoration was done with non-noble metals. The goal of this research was to discover green techniques for photocatalyst synthesis.

CHAPTER 2: LITERATURE REVIEW

This section provides a concise overview of various renewable hydrogen production methods, comparing them based on efficiency, cost, and environmental impact. Following this comparative analysis, the focus shifts to the fundamental principles of photocatalysis and the inherent limitations associated with current photocatalytic materials. Strategies such as cocatalyst loading and other techniques developed to overcome these limitations are also examined, highlighting the potential of photocatalysis and the gaps that remain in optimizing its performance. This discussion establishes the foundation for exploring innovative synthesis methods aimed at enhancing the performance of TiO_2 photocatalysts.

2.1 Hydrogen production methods from renewable sources

2.1.1 Electrolysis

Electrolysis uses electrical energy to split water into hydrogen and oxygen molecules. This process proceeds first by deionizing the water to prevent mineral deposition that could lead to undesired side reactions [27]. The passage of this current through the electrodes produces hydrogen and oxygen at the anode and cathode, respectively, as illustrated below.

Anode

$H_2O \rightarrow ½\ O_2 + 2H^+ + 2e^-$

Cathode

$2H^+ + 2e^- \rightarrow H_2$

Alkaline water electrolysis, solid oxide electrolysis, and Proton membrane electrolysis are some of the different technologies explored in this process. Alkaline water electrolysis and Proton membrane electrolysis have operating temperatures ranging from 50-80°C and operating pressure of 30 bars [16].

Solid oxide electrolysis, on the other hand, has an operating temperature in the region of 700-900°C. Therefore, its higher thermal demand requires a higher energy input. This limitation makes it unfavorable for large-scale applications compared to alkaline water electrolysis and proton membrane electrolysis. However, the cost of hydrogen produced from the promising technologies of underwater electrolysis is still higher than that generated from fossil fuels [9].

2.1.2 Photoelectrochemical (PEC)

A PEC system consists of an n-type photoanode for the oxygen evolution reaction (OER) and a p-type photocathode for the hydrogen evolution reaction (HER). In this system, the conduction band minimum and the valence band maximum need to be lower and higher than the water reduction potential and the oxidation potential, respectively, with an external bias applied to drive the redox reaction.

When the photoanode is illuminated with a light source, electrons and holes are generated. Electrons migrate through the external circuit to undergo HER at the counter electrode, while holes also migrate to the surface of the photoanode to carry out OER [6].

2.1.3 Photovoltaic-Electrochemical (PV-EC)

PV-EC is the coupling of a photovoltaic and electrochemical cell. The photovoltaic absorbs light to generate electricity, which is transferred to the electrochemical system to drive out HER at the cathode and OER at the anode, respectively. The EC system is only immersed in water, with the PV kept outside to prevent corrosion. It is a commercialized process with an efficiency greater than 18% [6].

2.1.4 Thermolysis

Thermolysis is the thermochemical splitting of water into hydrogen and oxygen at elevated temperatures around 2500°C. The primary concern of this process is the separation of the produced hydrogen and oxygen since their recombination can create an explosive mixture. Also, the exceptionally high temperature makes it challenging to construct a reactor that can withstand such temperatures [16, 28].

However, there are thermochemical cycles that make it possible for water splitting to be done at a relatively lower temperature below 1000°C. These thermochemical cycles also allow water splitting to be done in stages, which helps to solve the recombination of gaseous mixtures as well [16].

2.1.5 Biophotolysis

Biophotolysis is the production of hydrogen from water through a biochemical reaction using energy from the sun [29]. There are two types of Biophotolysis: direct and indirect biophotolysis.

Direct biophotolysis is the splitting of water into hydrogen and oxygen because of photosynthesis using hydrogenase, an enzymatic catalyst, under anaerobic conditions of cyanobacteria or microalgae. A positive feature of this process is that it occurs at ambient conditions.

REACTIONS

$H_2O \rightarrow \frac{1}{2} O_2 + H_2 + 2e^-$

$2H^+ + 2e^- \rightarrow H_2$

However, in indirect biophotolysis, carbohydrates build up during carbon dioxide fixing, producing oxygen, which is then replaced by hydrogen in the next stage. The substrate produced in the first stage serves as a carbon source for the next stage, so the media needs no additional nutrients [16].

2.1.6 Photocatalysis

Photocatalysis is the phenomenon in which electron-hole pairs are generated to carry out a redox reaction when a semiconductor is irradiated with a light source with energy more significant than the band gap [30]. When a semiconductor absorbs photons with energy equal to or greater than its band gap, holes, and electrons are produced, which undergo the hydrogen and oxygen evolution reaction at the conduction and valence band, respectively. Thermodynamics is essential to this process and, hence, needs to be satisfied before proceeding. The Gibbs free energy for this process is positive, which signifies that it is not a spontaneous reaction but requires energy to proceed. Also, the conduction band minimum of the photocatalyst should be lower than that of HER (H^+/H_2, 0V versus normal hydrogen electrode (NHE) and a Valence Balance Maximum (VBM) with potential energy more significant than that of the OER (O_2/H_2O, +1.23 V versus NHE at pH = 0) [6]

2.2 Comparison of various hydrogen production methods

In Song et al.'s Solar-Driven Hydrogen Production Methods: Recent Advances, challenges and Future Perspectives, he compared the conventional hydrogen production methods from fossil fuel sources with various solar-driven hydrogen production methods based on three critical metrics: efficiency, cost, and environmental impacts [6]. Here is a summary of the various processes under the cost, efficiency, and environmental impact metrics.

2.2.1 Efficiency

It is an index that measures the useful output by consumed input. Scientists desire to achieve efficiency that is close to unity. However, this is not easy to achieve. The efficiency of hydrogen produced from steam reforming and coal gasification, which are all sourced from fossil fuels, is 74-85% and 30-60%, respectively. Electrolysis, the most used renewable hydrogen production method, has an efficiency ranging from 55-80% [16].

Also, the efficiency of some of the leading solar-driven hydrogen production methods was ranked as follows: Photovoltaic Electrochemical systems (PV-EC) have the highest experimental efficiency, which is solar to hydrogen energy of 32%. Photoelectrochemical systems also have an efficiency of 19%. Photocatalytic and photobiological systems have efficiency of 1-3%. Solar thermochemical systems recorded the lowest efficiency of less than 1% [6].

2.2.2 Cost

Cost is an important yardstick for scaling up a process from the lab scale. Cost-effective processes are primal in all inventions; hence, cost analysis is done on all processes before their commercialization. Cost analysis is done to ascertain if a process is worth it or other alternate cost-effective processes can fulfill the same objective. Many factors are considered, including feedstocks, the main component of systems, energy conversion efficiency, balance of system expenses, and operating cost, among others.

Steam reforming and coal gasification are commercial processes; hence, it is easy to estimate the cost. The hydrogen produced through steam reforming costs US$1.83/kg-US$2.15/kg. Hydrogen produced using coal gasification costs US$1.77/kg-US$2.05/kg [7]. The cost of electrolytic means of hydrogen production is estimated at around US$4.15/kg-US$10.30/kg [7].

Finally, the cost of some solar-driven processes was estimated. This cost analysis was done using a rough estimate since most of these processes are still in their research stage, and most of their key components are unavailable in the market. Therefore, only a rough evaluation can be made. These projections provide insight into future hydrogen production. These estimations are called the levelized cost of hydrogen production [14-18].

The Levelized cost of hydrogen production of these processes includes LCOH for PV-EC - US$5.78/kg-US$23.27/kg, LCOH for PEC - US$2.9/kg-US$18.8/kg [11-12]. LCOH was calculated for photo-driven processes such as biophotolysis and photocatalysis, with efficiencies below 10% calculated based on this threshold for commercialization. Bio photolysis and photocatalysis have an LCOH of US$1.42/kgUS$2.13/kg and US1.60/kg, respectively [11,12].

The LCOH based on current reported STH efficiencies of about 0.7% is US$18.32/kg [14,15]. This value is ten times more than that produced from fossil fuels. However, with the realization of the 10% STH efficiency threshold, LCOH for PC, which is US$1.6/kg, is less compared with the LCOH for SRM and CG, which has an additional cost for CCS incorporated. This new LCOH for SRM and CG is US$1.93/kg-US$2.26/kg and US$2.24/kg-US$2.268/kg, respectively [6].

2.2.3 Environmental Impact

Environmental concerns have become a major consideration in process analysis due to the rise in global warming and other environmental issues. Efficiency and cost alone are not enough; ideal processes should also be environmentally benign.

H_2 is a clean fuel. However, processes and constructions used in its production can lead to the emission of greenhouse gases. Environmental impacts are assessed on two main indexes: the acidification potential and global warming potential. Global warming potential is assessed based on CO_2, N_2O, and CH_4 gas emissions. Acidification potential is measured from SO_X and NO_X

emissions. According to several studies on the environmental impacts on the various hydrogen production methods, SRM has the most prominent emissions and poses a significant environmental threat. Solar thermochemical processes have also been reported to exhibit significant emissions among solar-driven methods, primarily due to the use of CH_4, a carbon-based feedstock. Additionally, Photovoltaic-Electrochemical (PV-EC) processes have shown relatively high emissions of SO_2 and CO_2, largely attributed to the production of silicon photovoltaic panels. In contrast, Photocatalytic (PC) and Photoelectrochemical (PB) processes, which are also solar-driven, have been reported to exhibit low Acidification Potential and Global Warming Potential [6].

2.3 Fundamentals of photocatalytic water splitting

2.3.1 Photocatalytic procedures for splitting water using semiconductors

A semiconductor possesses an electronic band structure consisting of the Highest occupied energy band (valence band) and lowest empty band (conduction band) separated by a band gap. The generation of charge carriers is the fundamental principle for semiconductors in photocatalysis. Photocatalysis occurs in various steps in the following order such as (i)generation of charge carriers by light irradiation with photon energy more significant than the bandgap, (ii) separation and migration of generated charge carriers to the surface of the semiconductor, (iii) reduction and oxidation of water by photogenerated electrons and holes to produce hydrogen(H_2) and oxygen (O_2) respectively [31,32].

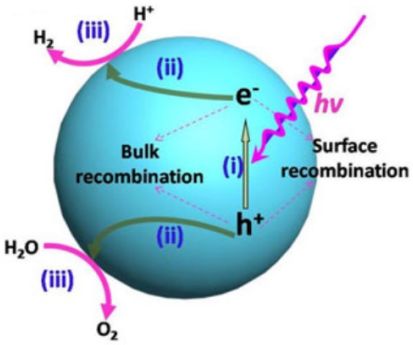

Figure 1: Schematic diagram of Photocatalytic Water Splitting Process. Reproduced with permission from ref. [31]

2.3.2 Thermodynamic requirements of photocatalytic water splitting

Photocatalytic water splitting is subjected to thermodynamic constraints, and therefore, the mere illumination and generation of charge carriers are insufficient for this reaction to occur.

This process is uphill; therefore, for this reaction to proceed, a Standard Gibbs free energy change ΔG° of 237kJ/mol is required.

Therefore, the suitable size of band gaps and positions of the conduction band minimum and valence band maximum must be considered. The semiconductor used in this process must have a more negative conduction band minimum than the reduction potential of H^+/H (0V vs. SHE at pH=0) and a valence band maximum more positive than (1.23V vs. SHE at pH=0).

$H_2O \rightarrow \frac{1}{2} O_2 + H_2$; $\Delta G^\circ = +237$kJ/mol, $E^\circ = 1.23$ eV (1)

$2H^+ + 2e^- \rightarrow H_2$ ($E^\circ_{RED} = 0$ eV) (2)

$2 H_2O \rightarrow 4H^+ + 4e^- + O_2$ ($E^\circ_{OX} = 1.23$ eV) (3)

Band gap (Eg,eV) = $\frac{1240}{\lambda}$ (4)

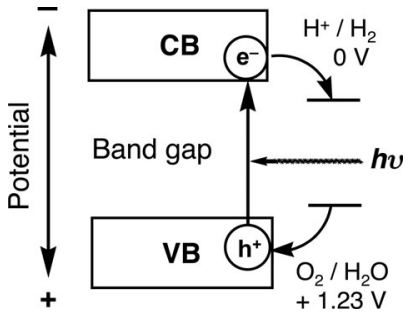

Figure 2: Thermodynamic requirements of photocatalytic water splitting. Reproduced with permission from ref. [32]

Extra photon energy is needed to overcome the energy barrier of 1.23 eV in order to achieve this nonspontaneous thermodynamic process, with the remaining being converted to chemical energy in products. Therefore, photocatalysts must have a band gap more significant than 1.23eV. The wavelength absorption should be less than 1000nm according to eqn 4 to achieve water splitting. Also, to utilize visible light, which accounts for about 43% of the solar spectrum, the band gap should be less than 3eV (i.e. edge wavelength of absorption more significant than 400nm) [31].

2.3.3 Semi-conductors used in photocatalytic water splitting

Since Honda and Fujishima used TiO_2 to split water over five decades ago, several photocatalysts have been explored, mainly because of the constraints of light absorption and recombination of charge carriers [33]. However, cost, toxicity, stability, and material scalability have also been considered [34]. TiO_2 is still widely used because of its wide band gap, low cost, chemical stability, and nontoxic nature.

Several other oxides, oxynitrides, oxysulphides, and metal-free semiconductors have been explored, and strategies such as doping, cocatalyst loading, and solid solutions, among others, have been used to increase their efficiency [9,10].

Photocatalysts can be grouped into wide band gaps, intermediate band gaps, and lower band gaps. Examples of wide band gap photocatalysts include TiO_2, ZnO, ZnS, and $SrTiO_3$, while those with intermediate band gaps include CdS, C_3N_4, and Ta_3N_5. Lower band gap photocatalysts include Cu_2O, WS_2, and MoS_2 [34].

An ideal photocatalyst should meet the criteria of optimum redox potential, broad wavelength absorption spectrum, photochemical stability, toxicity, and cost [33].

i. Redox Potential

Redox potential is the driving force behind redox reactions in photocatalytic processes. It is the difference between the conduction band and the valence band. For an ideal photocatalyst, the photocatalyst should have a conduction band well positioned to facilitate the reduction of protons to H_2(0.000 V vs. NHE at pH 0) and a valence band with more potential than that required to oxidize water into O_2 (1.23 V vs. NHE at pH 0) [34]. It is difficult for a photocatalyst to meet these stringent criteria. The high CB and deep VB positions can be illustrated by the fall of an object from a higher altitude to strike a ball at a lower position. This high acceleration and greater kinetic energy resulting from the increase in gravitational force on objects can be likened to the influence of redox potential on charge carriers [35].

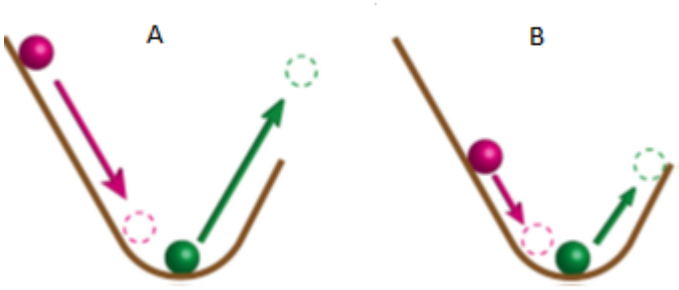

Figure 3: Similarity between gravitational potential energy and redox potential on charge carriers (a) fall from a higher altitude (b) fall from a lower altitude. Reproduced with permission from ref. [35]

ii. Wavelength light absorption

The solar spectrum comprises 52-55% infrared radiation, 42-43% visible radiation, and only 3-5% UV radiation [35-36]. Hence, there is a desire to produce a photocatalyst that uses a more significant proportion of the solar spectrum. However, most visible responsive photocatalysts have a lower band gap, so the driving force to drive the reaction is insufficient. Also, most are unstable, leading to deactivation over multiple cycles. Near-infrared responsive photocatalysts, although limited, do not generate reaction yield that is satisfactory as expected [34].

iii. Cost/Scarcity

Noble metals such as Ru, Pd, and Pt are some of the most used cocatalysts for photocatalytic water splitting. These noble metals exhibit very high efficiency. However, they are not ideal for large-scale applications due to their high cost and should be replaced by low-cost and abundant metals [34].

iv. Toxicity

In most photocatalytic reports, much emphasis has not been placed on toxicity, which has often been understudied or even neglected. The photocatalyst used should exhibit null toxicity or a high degree of biocompatibility [34].

v. Material scalability

The fabrication of an efficient photocatalyst may be done in a single-step or multiple-step process, which may be costly or not scalable. Also, recycling and reusability of the photocatalyst should be factored in when synthesizing a photocatalyst. For instance, a powdered photocatalyst dispersed in a large volume of liquid poses issues associated with recovery and reusability; hence, the configuration of the photocatalyst should also be considered in designing a scalable photocatalyst for real-world applications [34].

vi. Stability

The stability of a photocatalyst is essential in large-scale applications. This is done to assess the effect of the oxidation and reduction reaction on the photocatalyst. An ideal photocatalyst should last at least ten years. As a result, a reusability test should be performed to ensure its stability. Also, structure and morphological changes should be observed to understand the mechanism and changes in the photocatalytic performance [34].

2.3.4 Limitations in photocatalytic water splitting

The challenge of photocatalytic water splitting is that most photocatalysts used do not have the suitable band structure needed for the photocatalytic water splitting process, and also, even the materials capable of initiating the HER and OER at the conduction band and valence band have their efficiencies lower than and far from the efficiency required for commercialization of solar to hydrogen (STH) efficiency of around 10% [6]. The main reason for this limitation is that the essential stages for this process, such as harvesting light and generation of charge carriers, separation of charge carriers and transportation, and the redox reaction at the conduction and valence band, need to be more efficient.

However, a few photocatalysts, such as CdS and CdSe, satisfy these criteria but are plagued by photo corrosion, which leads to poor photostability[31].Intense efforts have been made to mitigate these limitations by continuously modifying existing photocatalysts and manufacturing new ones capable of addressing these limitations [38,39].

- Light harvesting

Light absorption is the initial stage in photocatalytic water splitting. The number and energy of photons absorbed by a semiconductor (photocatalyst) restricts the number of generated charge carriers. Consequently, efforts have been made to improve the light absorption properties of photocatalysts to absorb much of the sun's radiation in the visible region, which accounts for 43% of the solar spectrum [40, 41]. Band engineering, surface sensitization, and localized surface plasmon resonance effect are some measures used to improve the light-harvesting abilities of photocatalyst [31].

- BAND GAP ENGINEERING

Band gap engineering is modifying the electronic structure of a photocatalyst. Two main strategies are used in this modification, and they can be categorized into: cation or anion doping and the use of semiconductor alloys. Wide band gap photocatalyst (UV active) electronic structure can be modified to make it visible light responsive. Cationic doping is the introduction of impurity levels (donor level above the Valence band or acceptor level below the Conduction band) in the forbidden band to narrow the band gap of the photocatalyst [31].

Cation-doped photocatalysts do not always increase photocatalytic activity since the impurities introduced also act as a recombination site between the photogenerated charge carriers.

On the other hand, anion doping leads to the introduction of new VB positions and shifts the VB edge upwards to narrow the band gap and make it visible and light-responsive. Unlike cationic doping, anionic doping has fewer recombination centers, making it more effective for enhanced photocatalytic activity [31,42].

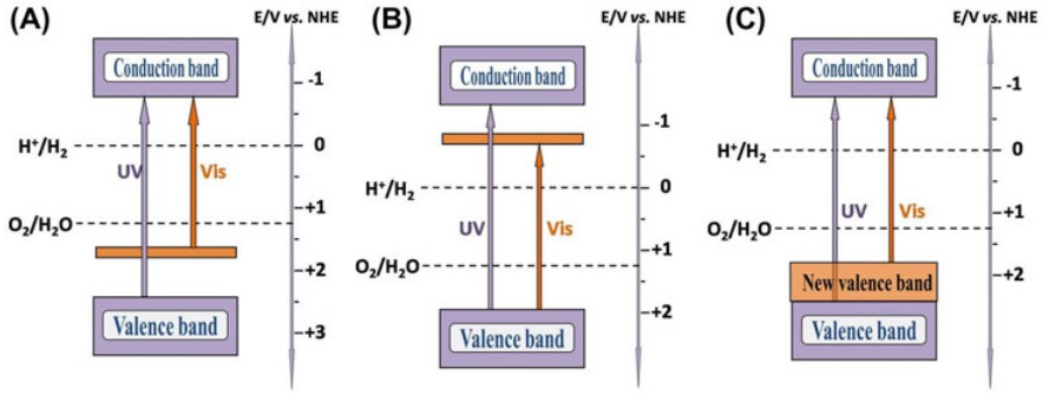

Figure 4: Band structure of cationic doping: (a) donor level above the valence band (b) acceptor level below the conduction band (c) band structure of anionic doping. Reproduced with permission from ref. [31]

A photocatalyst's band structure can also be modified by forming solid solutions between a wide and narrow band gap photocatalyst. To adjust or modify the band gap and position, the ratio of the composition of the narrow and wide band gap semiconductor in the solid solution is [31].

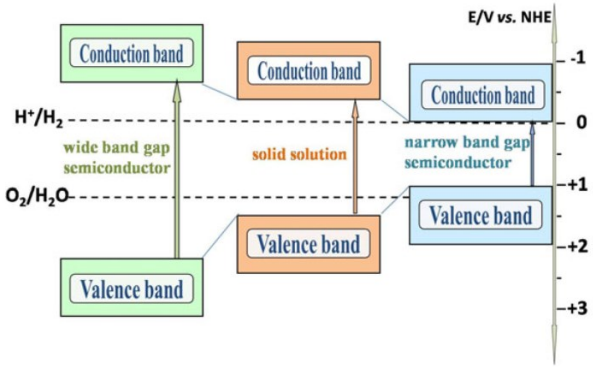

Figure 5: Band structure of an intermediate solution of a wide and low band gap semiconductor. Reproduced with permission from ref. [31]

- SURFACE ENGINEERING

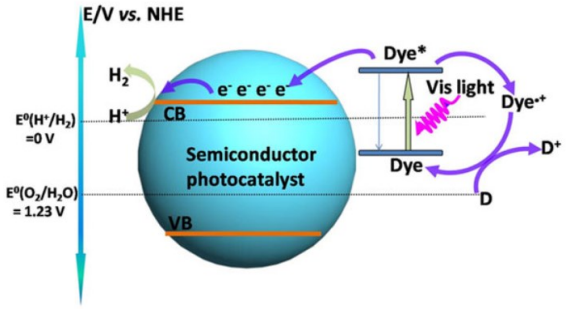

Figure 6: Schematic representation of the principle of dye sensitization. Reproduced with permission from ref. [31]

This mechanism was first used in 1991 to manufacture dye-synthesized solar cells. Since this report, much research has been done on this in photocatalytic applications. This mechanism involves the excitation of the dye molecule adsorbed on the surface of the photocatalyst. After absorption of visible light by the adsorbed dye molecule on the surface of the semiconductor to generate an excited state, electrons are injected into the semiconductor's conduction band. Dye is then reduced into a radical cation dye^+ on the surface of the photocatalyst. However, the radical cation dye^+ can be regenerated by reaction with electron donors from a sacrificial agent [31,42].

- Charge carrier separation

Aside from light harvesting, the separation and transport of charge carriers are essential for enhanced photocatalytic efficiency.

The recombination rate for the photogenerated electron-hole pairs occurs in the order of 10^{-9}s. In contrast, the redox reaction on the surface of the photocatalyst occurs in a much longer time of 10^{-8} -10^{-3}s [40]. To enhance the redox reaction occurring on the surface, the photogenerated charge carriers should be separated to prevent bulk or surface recombination. Recombination of photogenerated charge carriers happens due to the strong coulombic force between the photogenerated electron-hole pairs.

The short lifetime for the recombination of charge carriers to occur can be evidenced by comparing the coulomb constant (8.99 x 109 $N.m^2/c^2$) to the gravitational constant (6.67 x $10^{-11}N.m^2/kg^2$)

The coulombic constant is several magnitudes more significant than the gravitational constant. This substantial value of the coulombic constant is responsible for the rate at which the recombination of photogenerated charge carriers occurs [35].

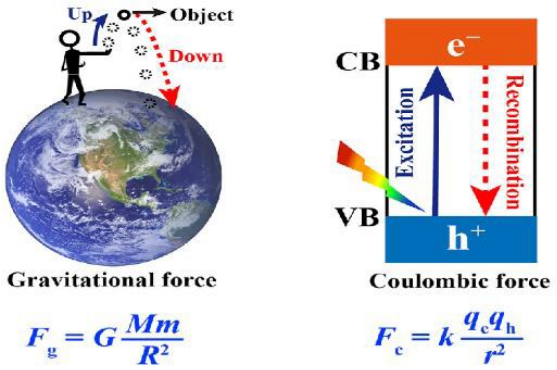

Figure 7: Schematic diagram of recombination of charge carriers to fall of objects under gravity. Reproduced with permission from ref. [35]

Some strategies to prevent the recombination of charge carriers and prolong their lifetime are semiconductor junctions, such as the formation of heterojunctions and the combination of semiconductors with graphene [31].

- HETEROJUNCTIONS

The heterojunction is the coupling of different semiconductors with suitable band structures to form a band bend at the junction. The band bend formation is caused by the difference in the chemical potential of the two different semiconductors. This band bend induces an inherent field that facilitates the spatial separation of charge carriers on different sides of the two photocatalysts by driving the photogenerated carriers to move in opposite directions[31,36].

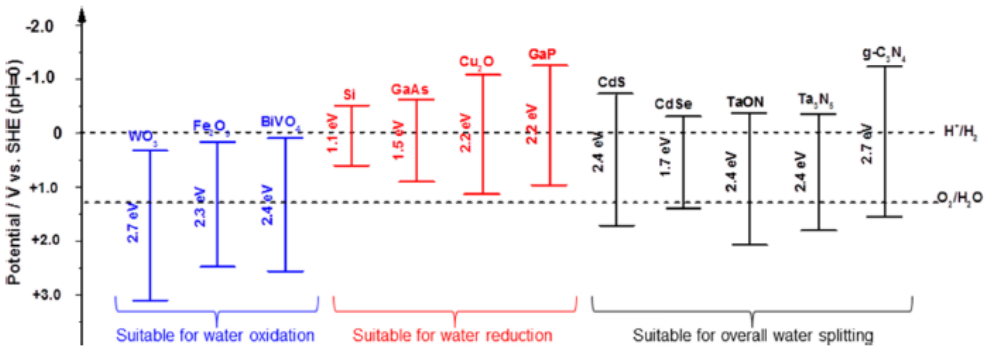

Figure 8: Band structure of varying suitable photocatalysts used in the photocatalytic water splitting process's oxidation, reduction, and overall water splitting. Reproduced with permission from ref. [36]

- TYPE (II) HETEROSTRUCTURE

Type (II) heterostructure consists of two photocatalysts: photocatalyst I (PC I) and photocatalyst II (PCII). Photogenerated electrons are transferred from PC I to PC II when light is irradiated on the photocatalysts. Concurrently, there is the transfer of holes in the opposite direction from PC II to the valence band of PC I [43-48].

However, the electron transfer between the photocatalysts is hindered by the existing electrons in the CB of the photocatalyst II due to repulsion between the existing electrons and the transferred photogenerated electrons. Likewise, the transferred photogenerated holes also encounter repulsion from the existing holes in the valence band of PC I.

Furthermore, the strong coulombic force between electrons and holes on a photocatalyst impedes the transfer of charge carriers [35].

The drawback of this type of heterostructure is that the transferred photogenerated electrons and holes, after reaching their target locations, possessed weak redox potentials to undergo reactions due to the repulsion [35].

- S-SCHEME

The s-scheme consists of a reduction photocatalyst and an oxidation photocatalyst. The reduction photocatalyst has a higher CB and VB position than the oxidation photocatalyst. However, it has a lower work function than the oxidation photocatalyst. Electrons in the RP spontaneously migrate to OP, which leads to electron depletion and electron accumulation layers near the interface in RP and OP, respectively, when the two photocatalysts are joined together. The OP is negatively charged, while the RP is positively charged. An internal electric field is formed that directs the transfer of electrons from OP to RP. The fermi energy of the two photocatalysts should be aligned to the same level. This alignment leads to a downward shift in the fermi levels of the OP and, conversely, an upward shift in the fermi levels of the RP.

Photogenerated electrons in the CB of the OP and holes in the VB of the RP recombine at the interface due to this band bending. This recombination due to the band bending can be understood by the downhill flow of water. The coulombic attraction between holes and electrons drives the recombination of the photogenerated electrons and holes at the OP and RP respectively at the interface.

Overall, the internal electric field, band bending, and coulombic attraction act as a driving force for the recombination of the unwanted charge carriers, leaving the potent photogenerated electrons and holes at CB of the RP and VB of the OP, respectively [35].

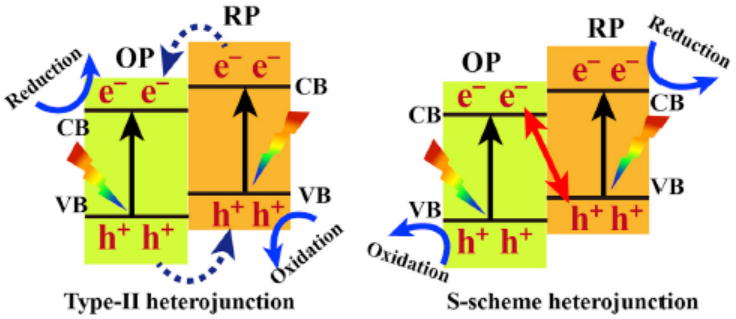

Figure 9:Schematic diagram of the Type ii(L) and S-scheme heterojunction(R). Reproduced with permission from ref. [35]

- Z-SCHEME

The natural photosynthetic process inspires the Z scheme. Bard was the first to report on this mechanism in 1979 [35, 55].

The Z scheme consists of two photocatalysts, PC I and PC II. The photogenerated electrons in the Conduction band of PC I and holes in the valence band of PC II are preserved due to their strong reducing and oxidizing abilities, respectively. The remaining charge carriers are then eliminated by the redox mediators.

In the traditional Z scheme, the pointless charge carriers are eliminated by redox ion mediators like $Fe^{3+/}Fe^{2+}$ and $I0_3^-/I^-$ [50-51]. The main drawback with the traditional Z scheme is that the redox mediator-induced back reactions are thermodynamically favorable and can take place quickly due to the consumption of the photogenerated electron and holes with substantial reducing and oxidizing abilities by the shuttle redox ion pairs. Light shield effect, feasibility confined in solution systems, slow charge carrier transfer rate, pH sensitivity of solution are some other limiting factors of the traditional Z-scheme [51].

The solid-state Z-scheme is an upgrade to the traditional Z scheme. Unlike redox ion pairs used in the traditional Z-scheme, an electron solid conductor is used as a charge carrier transfer bridge.

The choice of a suitable electron mediator is essential not only for charge transfer but also for stability. Noble metals such as Au and Ag have been used in this mechanism.

Graphene and CNT, because of their conductive nature, are suitable as electron mediators as well. The merits of this scheme over the traditional Z-scheme are the elimination of back reactions and its ability to function in both liquid and gas phases [36,52].

2.3.5 Cocatalyst

Cocatalyst provides the redox potential needed for the reaction at the photocatalyst's surface. Aside from the recombination of charge carriers, the redox potential needed to drive the reaction is essential. Most times, the redox reaction at the surface is too slow to consume the charges. When oxidation and reduction photocatalysts are loaded on photocatalysts, additional active centers are incorporated [31]. This loading helps drive the reaction at the surface and prevents back reaction [53-56]. Also, the stability of the photocatalyst is improved by how fast the charges are consumed, particularly with holes since they are responsible for photo corrosion [54], [57-59].

- Factors affecting the efficacy of cocatalysts

Cocatalyst loading plays a vital role in photocatalytic water splitting. However, some factors can hinder its role as a hydrogen and oxygen evolution cocatalyst. For instance, the loading amount size, and structure of the loaded particle can limit the activity of the loaded Cocatalyst.

Irrespective of the photocatalyst type, synthesis method, and loaded cocatalysts, a volcano-type trend exists between the amount of cocatalyst loading and the photocatalytic activity.

Loading a photocatalyst with a cocatalyst at the initial stage enhances its photocatalytic activity by improving the separation of charge carriers and providing active sites for gas evolution reactions. However, further loading of the photocatalyst above the optimal value leads to a substantial decrease in its activity.

The following factors are reasons for the decrease in activity due to high catalyst loading.

i) High loading of Cocatalyst blocks the active sites, thereby preventing water or a sacrificial agent from accessing them.

ii) excessive loading of Cocatalyst on the surface of the photocatalyst can shield the photocatalyst from incident thereby hindering the absorption and generation of charge carriers inside the photocatalyst.

iii)leads to the formation of large particle sizes, which leads to the loss of surface effects.

iv) Excess leading of Cocatalyst could introduce many charge recombination centers and, hence, decrease the photocatalytic activity

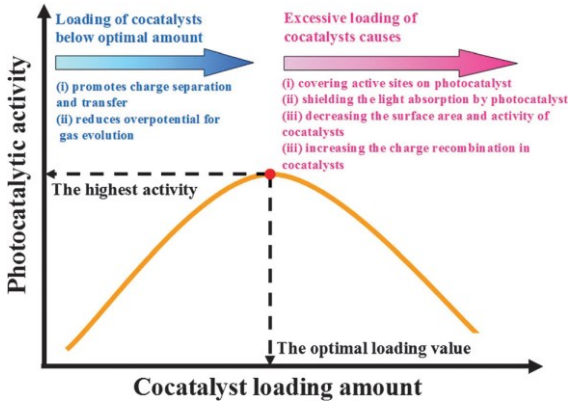

Figure 10: The volcano-type relationship between cocatalyst loading and photocatalyst activity. Reproduced with permission from ref. [10]

Also, the size of the Cocatalyst is another crucial factor in cocatalyst loading. Cocatalysts with small sizes have large surface areas and more active sites normally at the same loading amount.

Moreover, recombination of charge carriers is less likely to occur in a bulk small-size loaded particle than in a relatively large particle. Also, the exhibition of low barriers for interfacial charge transfer is profound in tiny particles in some cases. Small size and high dispersion of loaded particles enhances significantly the photocatalytic activity of a photocatalytic system, and this is evidenced by numerous research findings [65-69]

Lastly, the enhanced overall water splitting of the core shell structure of cocatalysts like Ni-NiO (NiOx) [65-68]and Rh-Cr_2O_3 [69], [70].This is a result of these core shells' ability to suppress the reverse reaction of H_2 and O_2 and limit the photoreduction of O_2 to shield the metal core from corrosion and ultimately enhance the robustness of the Cocatalyst.

- Transitional metals used as a cocatalyst

Transition metals are a viable option for large-scale applications because of their abundance and relatively low price. Most noble metals have been used as cocatalysts because of their electron-trapping abilities. Pt is the most efficient in trapping electrons due to its high work function. Some transition metals have been explored and used as cocatalysts and found to have good electron trapping ability. Nickel, for instance, has a higher work function than Au and Ag, which makes it very efficient in trapping electrons as well, as shown in Table 1 below. Other transitional metals such as Cu, Co, and Fe have all been explored as cocatalysts due to their electron trapping ability and ability to catalyze the reaction.

Metal	Work function
Pt	5.65[71]
Pd	5.12[72]
Au	5.12[11]
Ni	5.15[11]
Co	5.00[11]
Cu	4.65[11]

Table 1: Work function of some noble and transitional metals used as Cocatalyst

These metals play a role in separating the charge carriers by forming a Schottky junction with the semiconductor, leading to band bending at the interface of the contact between the semiconductor and the metal. Photogenerated electrons then migrate to the metal surface under the influence of electric field. For electrons to cross the barrier to the surface of the metal, they must possess a higher energy. When light is incident on the photocatalyst, photogenerated electrons with sufficient energy move from the CB of the photocatalyst to the surface of the Cocatalyst by crossing the Schottky barrier until there the fermi levels of the photocatalyst and the Cocatalyst are in equilibrium leaving the holes at the Valence band [73]. This migration helps in spatially separating the charge carriers (holes and electrons).

Cu, for instance, also plays an essential role in improving light absorption due to the LPSR effect [72,74]. The metal nanoparticle will have strong absorption when the inherent frequency of its electron matches that of the incident photon, leading to a collective oscillation of the electrons [73].

Transitional metal-based cocatalysts are mainly grouped into reduction and oxidation cocatalysts based on their charge-trapping abilities. Most of the reported transitional metal-based cocatalysts are on reduction cocatalysts. Reduction cocatalysts can be grouped as elemental metals (Ni, Cu, CoNi), metal sulfides (MoS_2, NiS), metal phosphides (Ni_2P, CO_3N), metal carbides (Ni_3C, MO_2C), metal borides (NiB and NiCoB), metal oxides (NiO, CuO), metal hydroxides ($Ni(OH)_2$ and $Cu(OH)_2$ [75].

Transitional metals	Examples
Elemental metals	Ni, Cu, CoNi
Metal sulphides	MoS_2, NiS
Metal phosphides	Ni_2P, CO_3N
Metal carbides	Ni_3C, Mo_2C
Metal borides	NiB, NiCoB
Metal oxides	CuO, NiO
Metal hydroxides	$Cu(OH)_2$, $Ni(OH)_2$

Table 2: Categorization of some of the various transitional metals used as reduction cocatalysts in PWS [75]

Categorization of some of the various transitional metals used as reduction cocatalysts in PWS [75] . The few reported cocatalysts used as oxidation cocatalysts include metals(Co, Mn) oxides(CoOx and MnOx), hydroxides ($Co(OH)_2$) and $Fe(OH)_3$, oxyhydroxides (FeOOH, CoOOH) and phosphates (Co-Pi, CoNi-Pi) [75]

Transition metals	Examples
Elemental metals	Co, Mn
Metal oxides	CoOx, MnOx
Metal hydroxides	$Co(OH)_2$, $Fe(OH)_3$
Metal oxyhydroxides	FeOOH, CoOOH
Metal phosphates	Co-Pi, CoNi-Pi

Table 3: Various groups of transitional metals used as oxidation cocatalysts in PWS [75]

- Cocatalyst Loading Methods

Photocatalysts have been loaded with cocatalysts using varying methods. These methods used can be grouped into direct addition loading and composite loading.

- DIRECT ADDITION LOADING

Direct addition loading is the direct addition of precursor on the surface of a photocatalyst to grow the Cocatalyst (nanoparticle) on the surface. This type of loading leads to the formation of a tight interface between the photocatalyst and Cocatalyst. Again, this method allows for the controlling of the loading site, particle size, and distribution of the Cocatalyst on the substrate(photocatalyst). Also, layer-by-layer loading can be used in the formation of unique structures such as core-shell structures. Solvothermal treatment, precipitation, immersion, photo deposition, hydrothermal treatment, microwave treatment, inkjet printing, and so on are direct addition loading methods [11].

- COMPOSITE TYPE LOADING METHOD

This type of loading begins by synthesizing the desired Cocatalyst and then loading it into the photocatalyst. The synthesized Cocatalyst can be loaded by impregnation, physical mixing, grinding, and others. The merits of this loading method are that the photocatalyst does not restrict the Cocatalyst's synthesis conditions, and the Cocatalyst's microstructure can be precisely controlled [11].

To sum it up, the literature review(Chapter 2) briefly discussed and compared renewable hydrogen production methods, focusing on their efficiency, cost, and environmental impact. It also examined the potential of photocatalysis, mainly if the STH efficiency of 10% is realized, as a promising method for hydrogen production.

The fundamentals and limitations of photocatalysis were discussed, along with some solutions to improving the light harnessing ability and charge carrier separation. Cocatalyst loading was discussed as one measure to help solve this limitation. However, most loading methods often require an extensive amount of solvent and are energy-intensive.

In the next chapter (Chapter 3), Cu and Ni were uniformly decorated on titania nanotubes using microwave to address this limitation. The effect of the precursors' concentration and reaction parameters like temperature and time was studied to determine the best and most efficient catalyst, considering the amount of solvent or reagent used, energy, and time.

CHAPTER 3: MICROWAVE-DRIVEN DECORATION OF CuNi/TiO2 FOR HYDROGEN PRODUCTION

3.1 Introduction

The demand for energy has significantly increased in recent decades, driven by population growth and rising living standards worldwide. Energy consumption has surged by over 50% in the past fifty years.[76], and projections indicate a further 30% rise by 2040 [77]. With the global population expected to reach 8.5 billion by 2030, 9.7 billion by 2050, and an estimated 11.2 billion by 2100[78], the demand for energy resources is anticipated to increase significantly in the foreseeable future.

Presently, fossil fuels constitute the primary source of global energy supply. However, their non-renewable nature and environmental impact necessitate urgent exploration of sustainable and renewable energy alternatives. Solar energy emerges as a promising solution owing to its abundant availability. Despite only a minute fraction of the sun's energy reaching Earth, it amounts to 120,000 trillion Watts per hour, capable of meeting global energy demand annually [79].

Multiple solar-powered technologies have been developed, among which photocatalytic water splitting holds promise as a standout alternative. This process harnesses sunlight to produce hydrogen, a highly versatile energy carrier characterized by its high energy density and convenient storability, which are essential for mitigating solar intermittency [3-4]. Hydrogen combustion yields only water vapor, establishing it as a clean energy option with zero greenhouse gas emissions [5].

Despite its potential, photocatalysts like titanium dioxide (TiO_2) are constrained by limitations such as narrow absorption of the solar spectrum and rapid recombination of photoinduced charge carriers. Titanium dioxide, with its wide band gap of 3.2 eV, predominately absorbs ultraviolet radiation, which accounts for only 3-5% of incident solar radiation [35-36].

TiO_2, first utilized by Honda and Fujishima in 1972 to split water, is the most commonly used photocatalyst in photocatalysis [8]. Its chemically stable, nontoxic, and environmentally benign nature makes it ideal [80], [81]. Consequently, various morphologies have been explored with modifications aimed at increasing absorption and extending the lifetime of charge carriers. Titania nanotubes have been extensively studied due to their high aspect ratio and controlled charge transfer in a defined direction [82].

The synthesis of TiO_2 nanotubes has been achieved using diverse methods, such as hydrothermal, template, solvothermal, and electrochemical anodization [83]. Electrochemical anodization has emerged as a compelling method for producing ordered and aligned nanotubes with a high aspect ratio [84]. Furthermore, this method allows for precise control over the dimensions of the nanotubes by adjusting key parameters such as voltage, electrolyte composition, pH, and anodizing time [83], [84].

Early studies by Zwilling et al. (1999) [85] and Grimes et al. (2001)[86] demonstrated the formation of self-organized TiO_2 nanotubes using fluoride-based and H_2O-HF electrolytes, respectively. The advantages of electrochemically grown self-organized TiO_2 nanotubes extend to their ease of recovery and reusability compared to nanoparticles or nanotubes prepared via alternative methods, facilitating practical applications in photocatalysis.

Furthermore, photocatalyst performance can be effectively enhanced by depositing metal co-catalysts onto TiO_2 surfaces. While noble metals like Au, Pd, Ru, and Pt have demonstrated exceptional catalytic properties, their limited availability and high cost have steered attention towards more abundant and cost-effective transition metals such as Cu, Ni, and Co [78]. These transition metals possess high work functions and can catalyze the hydrogen evolution reaction (HER). Deposing these transition metals onto photocatalysts enhances charge separation efficiency, decreases overpotential, creates active sites for the HER, and improves light absorption [78]. Various techniques have been utilized for decorating photocatalysts with these cocatalysts. Microwave-assisted deposition has emerged as a sustainable choice among these methods due to its minimal solvent utilization and energy consumption. Moreover, this approach allows uniform heating and precise control of crucial reaction parameters [87].

In this project, titania nanotubes were decorated with copper and nickel via microwave decoration by optimizing the various reaction conditions and investigating the synergistic effect between copper and nickel. This work aimed to lay the foundation for green, sustainable, and economical hydrogen production methods.

3.2 Experimental section

3.2.1 Materials

Nickel (II)chloride hexahydrate,99.3%(Thermo Scientific), Triethanolamine (Thermo Scientific), trimethylene glycol,99%(Thermo Scientific), Ammonium fluoride(Fischer chemical), Titanium foil 99.7% (Strem Chemicals, INC), Copper (II) Chloride,99%, extra pure, anhydrous (Thermo scientific)

3.2.2 Growth of titania nanotubes

Titanium foils (Strem catalog, 0.127mm thickness, 99.7% purity) were degreased by sonicating in acetone, ethanol, and distilled water in that order and dried in the air. The foils were then anodized in triethylene glycol (TEG) electrolyte containing NH_4F (0.30M) and H_2O (3wt%) at 60 V for 30 minutes. XANTREX DC power supply was used to supply the DC potential. The anodized titania foil was soaked in ethanol and dried under an air stream. After drying, TiO_2 was annealed at 450°C in air for 1 hr using a Thermolyne oven (Thermoscientific) with a heating rate of 10°C/min.

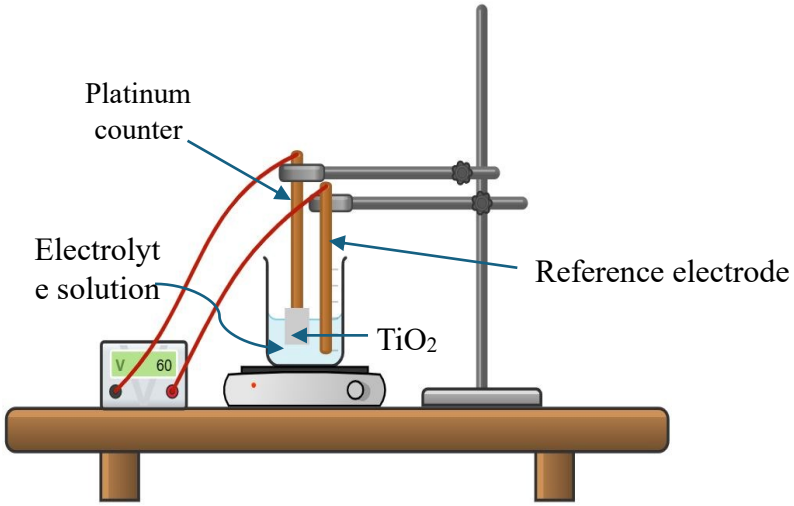

Figure 11: Schematic diagram of the electrochemical anodization of titanium foil

3.2.3 Decoration of Cu and Ni nanoparticles

The TiO_2 nanotubes were decorated with copper and nickel via microwave deposition using a microwave reactor (CEM Discover 2.0). The titania nanotubes were placed in a reactor vial and decorated using varying concentrations of 12.5 (Cu-12.5/TiO_2), 25 (Cu-25/TiO_2),50 (Cu-50/TiO_2), and 100 mM (Cu-100/TiO_2) $CuCl_2$ precursor 12.5 (Ni-12.5/TiO_2), 25 (Ni-25/TiO_2), 50 (Ni-50/TiO_2) and100 mM(Ni-100/TiO_2) in 10 mL of ethanol for $CuCl_2$ and $NiCl_2.6H_2O$ precursors respectively in a glass reactor vial. The reaction conditions for the initial stage were a reaction time of 10 minutes and a temperature of 100°C. The CuNi mixture(Cu-25Ni-12.5/TiO_2) is formed from 12.5 mM of $NiCl_2.6H_2O$ (Ni-12.5/TiO_2) and 25 mMof $CuCl_2$ (Cu-25/TiO_2), the concentration resulting in the most active photocatalyst, was also decorated with the same initial condition (10 minutes and 100°C). The best photocatalyst among Cu, Ni, and CuNi was then decorated with other temperature and time variations of 75, 125, and 150°C and 5, 10, 15, and 20 minutes, respectively.

After decoration, the decorated TiO_2 is rinsed thoroughly with ethanol, followed by distilled water, and dried using air.

3.2.4 ICP-MS preparation

Soak samples decorated samples are to be analyzed using 20% nitric acid for about 8 hours. After soaking, the solution was quantitatively transferred to a 10 ml volumetric flask. Top up the volume with deionized water.

The dry foil was weighed before and after the decoration to observe any significant difference in weight. There was no significant change in the mass of the samples. If there is a significant change in mass, it is recommended to dilute the sample to ensure that the total dissolved content is less than 1000 µg/mL.

3.2.5 Characterization

The crystal phase of the TiO_2 nanotube was examined using a benchtop powder X-ray Diffraction (XRD) instrument with a Hypix-400MF 2D hybrid pixel array detector (HPAD) at room temperature. The morphology of the photocatalyst was studied using a REGULUS 8230 Scanning Electron Microscope.

Thermo Scientific Talos F200X G2(S) TEM was used to examine the decorated TiO2 photocatalysts' elemental mapping and HR TEM for interplanar distance. The surface chemistry of the TiO2 nanotube was observed using Thermo-scientific K-Alpha.

Finally, the UV Vis diffuse reflectance spectra were recorded using Carry 5000 UV-Vis NIR from Agilent Technologies, where an annealed Ti foil was used as the standard reflectance. The photocatalyst was examined at room temperature from a 250-800nm wavelength.

3.2.6 Photocatalytic test

Photocatalytic experiments were conducted in a 50 mL quartz reactor with 1 ml of TEOA and 9 mL of water. TEOA is added as a scavenger to scrub off the photogenerated holes, which may interfere with the reaction. Before the photocatalytic test, the reactor, containing TiO_2 nanotubes and water-TEOA mixture, is purged with nitrogen to eliminate air, which may interfere with the response and react with the photogenerated electrons. After purging, the reactor is irradiated with UV radiation from a customized 4 UV LED cell with an average power of 145 mW (λ=358 nm) in an enclosed box for 4 hours.

Consequently, after the reaction, the products are analyzed by a gas chromatograph (Clarus 590 GC) with nitrogen as the carrier gas.

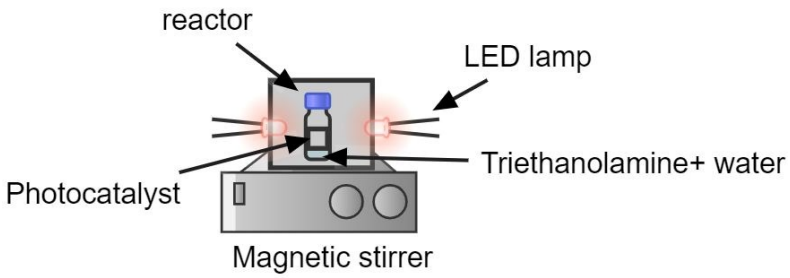

Figure 12: Schematic diagram of the photocatalytic test setup

3.3 Results and Discussion

The phase composition of the annealed Titania nanotube was analyzed using a Benchtop Powder X-ray Diffraction (XRD) instrument with Hypix-400 MF 2D hybrid pixel array detector (HPAD) together with a 600 W X-ray source, and the results can be seen in fig 1. The sample showed an intense peak around 25.3°, indicating the anatase phase formation. Also, the decorated TiO_2 was analyzed, but no additional peak corresponding to the copper, nickel, or its oxide phases was detected. The peak profile remained the same as the bare TiO_2 nanotube, indicating that the particle size of the metals and their amounts might be too small to be detected.

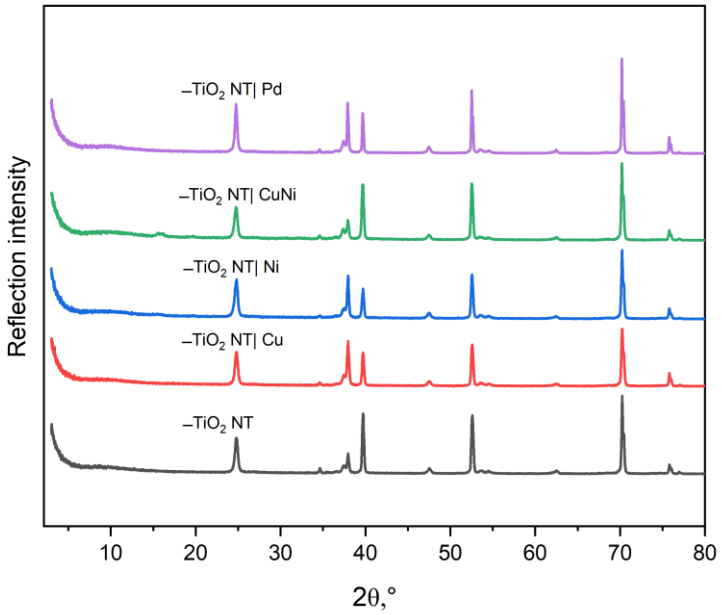

Figure 13: XRD analysis of the bare TiO_2 nanotube and the various decorated TiO_2 nanotube

The morphology of the titania nanotube was observed using REGULUS 8230 Scanning Electron Microscope, and the results can be seen in Fig 1 below, which shows ordered and aligned spaced titania nanotubes. The length of the tube was found to be around 3 μm and a diameter of around 200 nm. Again, the morphology of the various decorated samples was also analyzed after microwave treatment, and there was no noticeable difference between the fresh TiO_2 nanotube and the decorated nanotube. This also suggests that the particle size of the decorated metals is too small to be detected by SEM analysis.

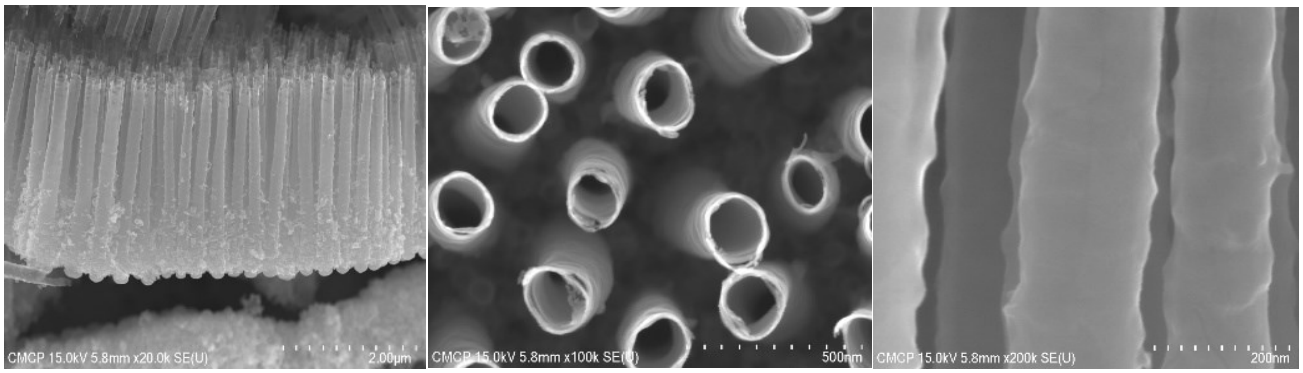

Figure 14: SEM images of TiO_2 nanotube

Subsequently, ICP MS was done using ICP 7500ce (Agilent Technologies) to evaluate the efficacy of the microwave deposition. The loading of the metals on the nanotube's surface was analyzed for different concentrations of copper to observe the correlation between the concentration of the precursor solution used and the loading. $CuCl_2$ solution with varying concentrations of 12.5 mM, 25 mM, and 50 mM resulted in loadings of 42.990 µg, 55.170 µg, and 373.500 µg, respectively, for Cu. This confirms the presence of the deposited metals on the surface of the TiO_2 nanotubes. Also, it can be observed that the loading concentration increased with the increase in the concentration of $CuCl_2$ solution used.

Photocatalyst	Cu loading(µg)	Ni loading(µg)
Cu-12.5/TiO_2	42.990	-
Cu-25/TiO_2	55.170	-
Cu-50/TiO_2	373.500	-
Ni-12.5/TiO_2	-	3.039
Ni-100/TiO_2	-	4.269
Cu-25Ni-12.5/TiO_2	8.946	0.804

Table 4: ICP-MS results for Cu and Ni decorated TiO_2 nanotube

Moreover, Thermo Scientific Talos F200X G2 (S) TEM was used for EDS mapping analysis (Fig 15) and HR TEM (Fig 16) to determine the dispersion of the decorated metal nanoparticles on the titania nanotubes and changes in the morphology of TiO_2 nanotubes after decoration. Traces of very small copper and nickel nanoparticles were evenly dispersed on the nanotubes and in the spaces between them.

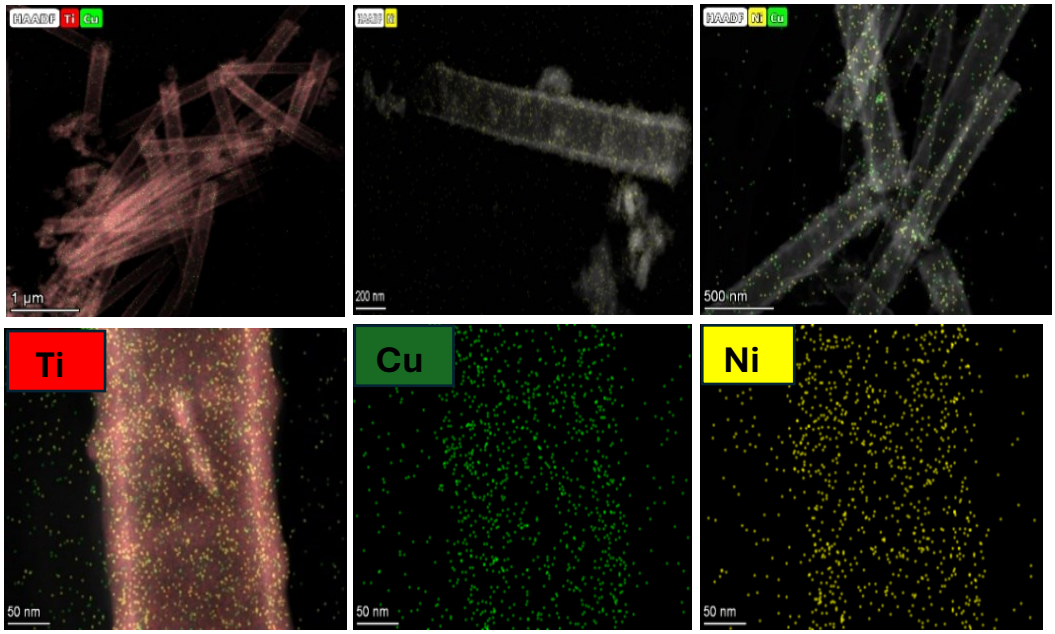

Figure 15: EDS mapping of decorated TiO_2 nanotube

The decorated TiO_2 HR TEM (Fig 16) was also analyzed to determine any additional phases of the TiO_2 or decorated metal nanoparticles or changes in the interplanar distance that can result from these small particles occupying interstitial spaces in Ti or creating defects in the Titania structure. The interplanar distance was ~ 3.4Å, corresponding to (101) anatase phase crystallographic plane, further confirming the results from the XRD spectra [88,89].

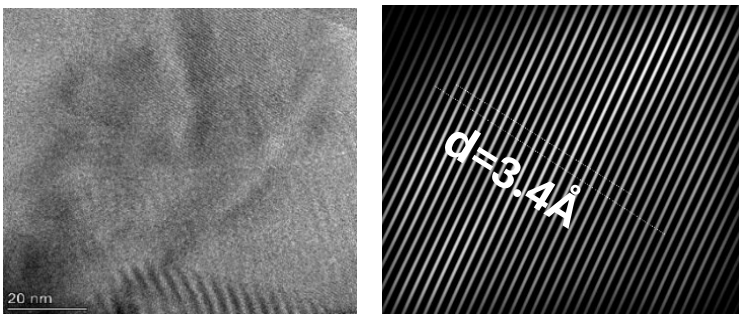

Figure 16: HR-TEM and interplanar distance of TiO_2

Furthermore, XPS analysis was done using Thermo-scientific K-Alpha to determine the chemical state of elements present on the surface of the TiO_2 nanotube for all the decorated samples. It is observed that the surface chemistry of the titanium (IV) oxide reveals a single state, which is characteristic of Titanium (IV) oxide of Ti 2p 3/2 peak energy of around 459.3eV (Fig. 17a) [90], [91]. This confirms that the microwave decoration process did not alter the structure of the TiO_2. Again, the constant binding energy observed also validates that the decoration occurred on the surface only and that there was no doping.

Fig 17c shows the XPS analysis for the decorated Cu/TiO_2. The spectral analysis of the Cu 2p 3/2 reveals a peak energy of ~933eV, which is one of the chemical states of copper and characteristic of Cu(0) metal [12], [92].

Also, (Fig. 17d) shows the spectral analysis for Ni/TiO_2 which shows peak of 856.5eV for Ni 2p 3/2 which is characteristic of Ni^{2+} [93], [94].

The oxygen spectral shows O 1s peak at 530.5eV and ~531.9eV, which is characteristic of the O in TiO_2 and $Ni(OH)_2$, respectively [93, 95]. This suggests that $Ni(OH)_2$ decoration was obtained on the surface of the TiO_2 nanotube. The formation of nickel hydroxide could be due to the reaction between nickel and adsorbed water molecules on TiO_2 (Fig. 17b) [92, 95]. Also, the precursor contained free water molecules that could be dissolved in the ethanol. This hydroxyl group could react with the nickel (II) to produce $Ni(OH)_2$. This reaction was more favorable than the reduction of the Ni (II) ions, hence the resulting observation. This could be justified because ethanol is a weak reducing agent, and therefore, lowering conditions needed for reduction might be weaker than the energy required for the formation of $Ni(OH)_2$. On the other hand, the decrease in the intensity of the oxygen in the decorated TiO_2 nanotube spectra compared to that of the pure TiO_2 nanotube can be evidenced by the decoration or shielding of the $Ni(OH)_2$ loading.

Finally, the XPS spectra for the bimetallic decoration of $CuNi/TiO_2$ were studied (Fig. 17 e, f &g). The Ni (II) spectra peak characteristic of Nickel hydroxide was observed, and the identical spectra signal obtained for the Ni/TiO_2 was observed in the bimetallic decoration (Fig. 17f). The oxygen spectral for the $CuNi/TiO_2$ was then analyzed without additional signal. However, the XPS signal for the $Ni(OH)_2$ was still observed. This frther confirms our observation that the surface chemistry of the nickel remained unchanged in the mixture. Nonetheless, a new spectra signal was identified in the copper spectra (fig17g). This peak of ~933.3eV for Cu 2p 3/2 was determined to be characteristic of the CuO spectral signal.[96], [97].

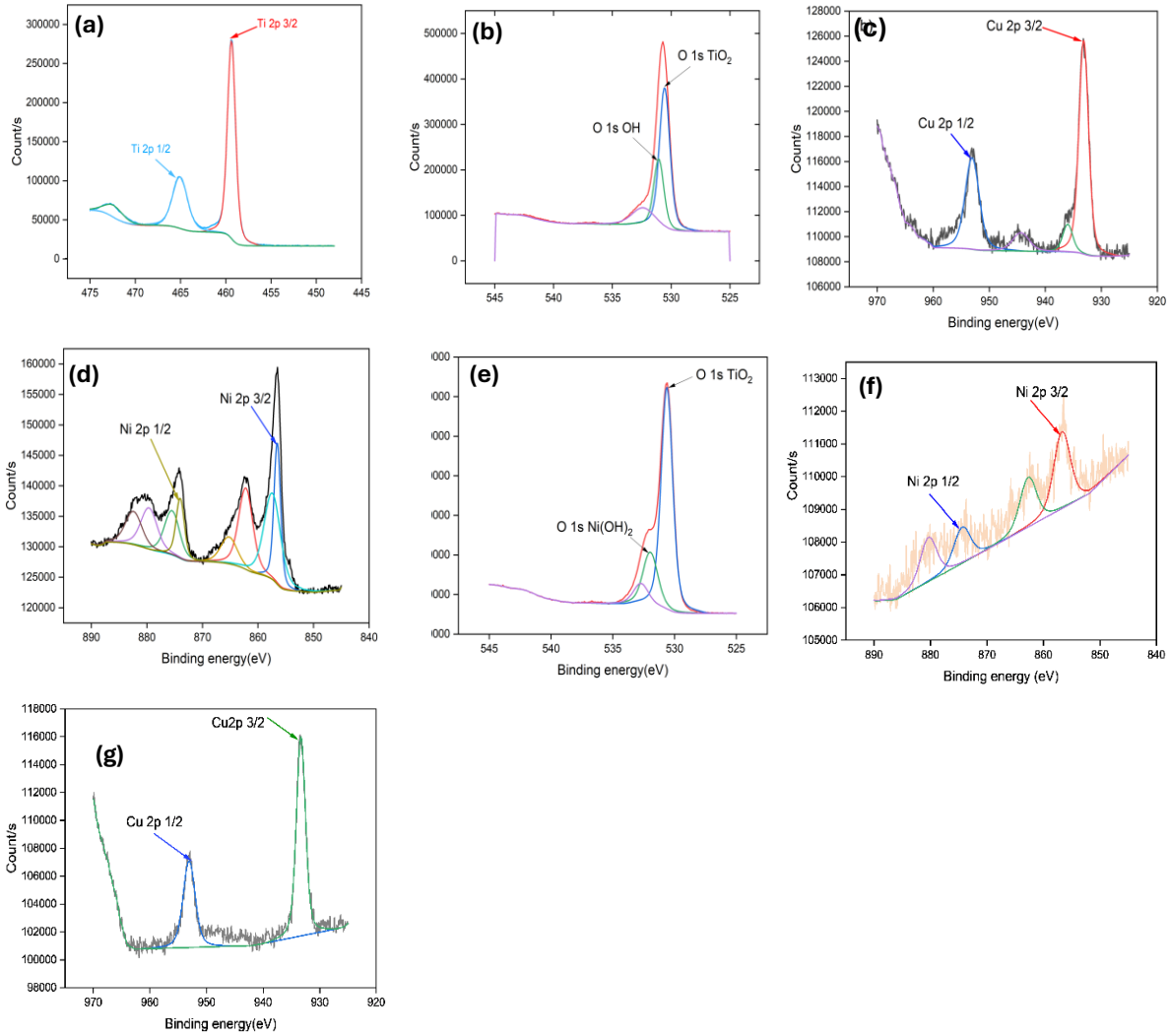

Figure 17: (a & b) XPS signal of Ti and O in TiO_2 (c) Cu XPS spectrum in Cu/TiO_2 (d) XPS signal of ni in Ni/TiO_2 (e) O 1s signal of $Ni(OH)_2$ and TiO_2 in $CuNi/TiO_2$ (f) XPS signal of Ni in $CuNi/TiO_2$ (g) Cu XPS spectrum in $CuNi/TiO_2$

To sum up, Carry 5000 UV-Vis NIR from Agilent Technologies was used for the UV-VIS DR study to evaluate the optical properties of the bare TiO_2 nanotube and the various decorated TiO_2 samples using an annealed titanium foil as a reference (Fig. 18)

The spectra region was from 200 nm to about 800 nm. However, some portions were cut off due to excessive noise in the preceding areas. It can be observed that the reflectance of TiO_2 increased gradually to around 389 nm and then began to decrease. This decrease in the reflectance around 400nm can be associated with the increase in the light absorption by TiO_2 (band gap of 3.2 eV) due to the electron interband transition of TiO_2 [92, 98]. The absorption peak around 600 nm in the visible spectrum can be attributed to the low-content carbon impurities in the layers [99]. The improved absorption of Ni/TiO_2 can be explained by the d-d transition of Ni(II) [98, 100]. Above ~400 nm, Cu/TiO_2 is known for its good absorption due to surface plasmon resonance, with a characteristic peak around 600 nm.[92, 101].

Overall, CuNi showed much better absorption in the UV and visible regions. This enhanced absorption is due to the cooperative abilities of the Cu-containing compound and the Nickel-containing compound. Notably, copper oxides also exhibit surface plasmon effects, hence the observance of the characteristic peak around 600 nm.[102].Again, the absorption above ~450 nm in CuNi/TiO2 is characterized by the d-d transition of Cu(II) (CuO) which is present in the mixture.[92, 103]. Again, this stronger absorption in the visible region can be associated with a narrow band gap of CuO, which is ~1.8 eV[104]From the spectra, it is evident that Ni/TiO_2 showed a better absorption in the UV-ViS range from around 400-525 nm, while Cu showed even a much higher absorption around 600 nm, with ~60% absorption of the visible light. Hence, this cooperative absorption ability of $CuNi/TiO_2$ can be justified by the unique absorption abilities of the individual components of the alloy.

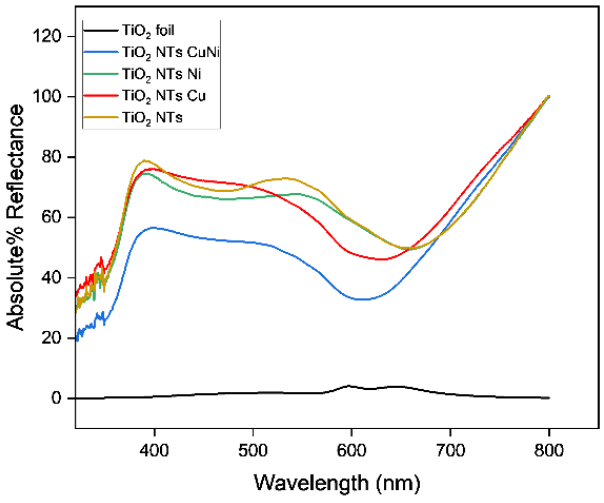

Figure 18:UV-Vis diffuse reflectance spectra of bare TiO_2, Cu/TiO_2, Ni/TiO_2 and $CuNi/TiO_2$ photocatalysts

Finally, a photocatalytic test was conducted to assess the activity of the various decorated photocatalysts. First, photocatalytic tests for the individual mono metallic photocatalysts (Cu/TiO_2 and Ni/TiO_2) were performed by varying concentration and keeping temperature and time constant. The ideal concentration that yielded the best activity was $Cu\text{-}25/TiO_2$ with HER of 0.821 $\mu mol/cm^2$. h (Fig. 19a). $Ni\text{-}12.5/TiO_2$ also gave the best activity with HER of 0.725 $\mu mol/cm^2$. h (Fig. 19b). The optimum copper and nickel loading that yielded the best activity was ca. 55.17 µg and ca.3.04 µg per sample, respectively. The ideal loading and uniform dispersion of the metal nanoparticles can explain the enhanced activity by the two best photocatalysts. It can be observed that higher concentrations resulted in decreased activity, which can be attributed to the fact that there was an aggregation of the metal nanoparticles or shielding of the TiO_2 surface as a result of excessive loading, which hindered incident light from getting to the TiO_2 surface, thereby limiting the amount of generated charge carriers [10].

Notably, the control test was done in the same conditions without light, and no hydrogen was produced. Again, water and TEOA with no photocatalyst were subjected to the same incident light radiation for the same duration, and there was no HER(Fig. 19e). This was done to ensure that the hydrogen produced was only from the water-splitting process. Bimetallic loading of the most active monometallic photocatalysts was made using the same precursor concentrations. This was done to harness the synergistic effect of the various transitional metals. Nickel has a high work function comparable to some noble metals and forms a Schottky barrier with the photocatalyst, which helps in the spatial separation of charge carriers by preventing recombination of charge carriers and back reactions. On the other hand, Cu-containing compounds exhibit a surface plasmon resonance effect and help exhibit enhanced absorption, particularly in the visible region. The impact of this cooperative effect is observed in the activity of $CuNi/TiO_2$. A substantial activity of 1.426 $\mu mol/cm^2$.h was observed (Fig. 19e). The individual loadings of Cu and Ni in the mixture were ca.8.946 µg and ca.0.804 µg per sample, respectively. The minimum loading of Ni shows a strong affinity between TiO_2 and Cu. This can be explained by the standard reduction potential of copper(+0.34 V) and Ni(-0.25 V) [13]. The positive potential of copper makes it favorable for gaining electrons to be reduced; hence, the reduction reaction is more profound for Cu/TiO_2 than that of Ni/TiO_2.

Similarly, the temperature was varied for the $CuNi/TiO_2$ photocatalyst, and temperature @125 ºC yielded the best activity of 2.40 $\mu mol/cm^2$. h (Fig. 19c). This suggests that an optimum loading was obtained at @125 ºC. A further increase in the temperature to 150 ºC resulted in a lower activity of 1.133 $\mu mol/cm^2$.h, which can be justified by excessive loading at that temperature.

Lastly, the ideal time that yielded the best activity for the $CuNi/TiO_2$ was 10 minutes, suggesting that the best loading was at 10 minutes with an activity of 1.426 $\mu mol/cm^2$. h (Fig. 19d). After the best time of 10 minutes, the photocatalyst's activity began to decrease, which can be attributed to aggregation of the deposited nanoparticles, shielding effect, or creation of recombination centers due to excess loading [10].

It is noteworthy that Pd/TiO_2, a proven and effective noble cocatalyst also synthesized at the same conditions with a loading of ca. 5.308 µg, yielded an activity of 0.477 $\mu mol/cm^2$. h. The activity for the bare TiO_2 nanotube was 0.103 $\mu mol/cm^2$. h. The activity of the best photocatalyst at the same condition, CuNi, was ca. 14 times higher than that of the bare TiO_2 nanotube. Again, $CuNi/TiO_2$ was ca. three times more active than Pd/TiO_2.

However, the concern with CuNi/TiO_2 was that it was unstable, as seen in (Fig 20). The stability test was done in four cycles: washing the photocatalyst, drying and replacing the water and TEOA, and purging again with nitrogen, which was done before each cycle. This instability could be associated with CuO photo corrosion since it has been reported to be susceptible to photo corrosion [105], [106], [107]. Also, the metals might leach into the solution because they are not properly bound to the nanotube.

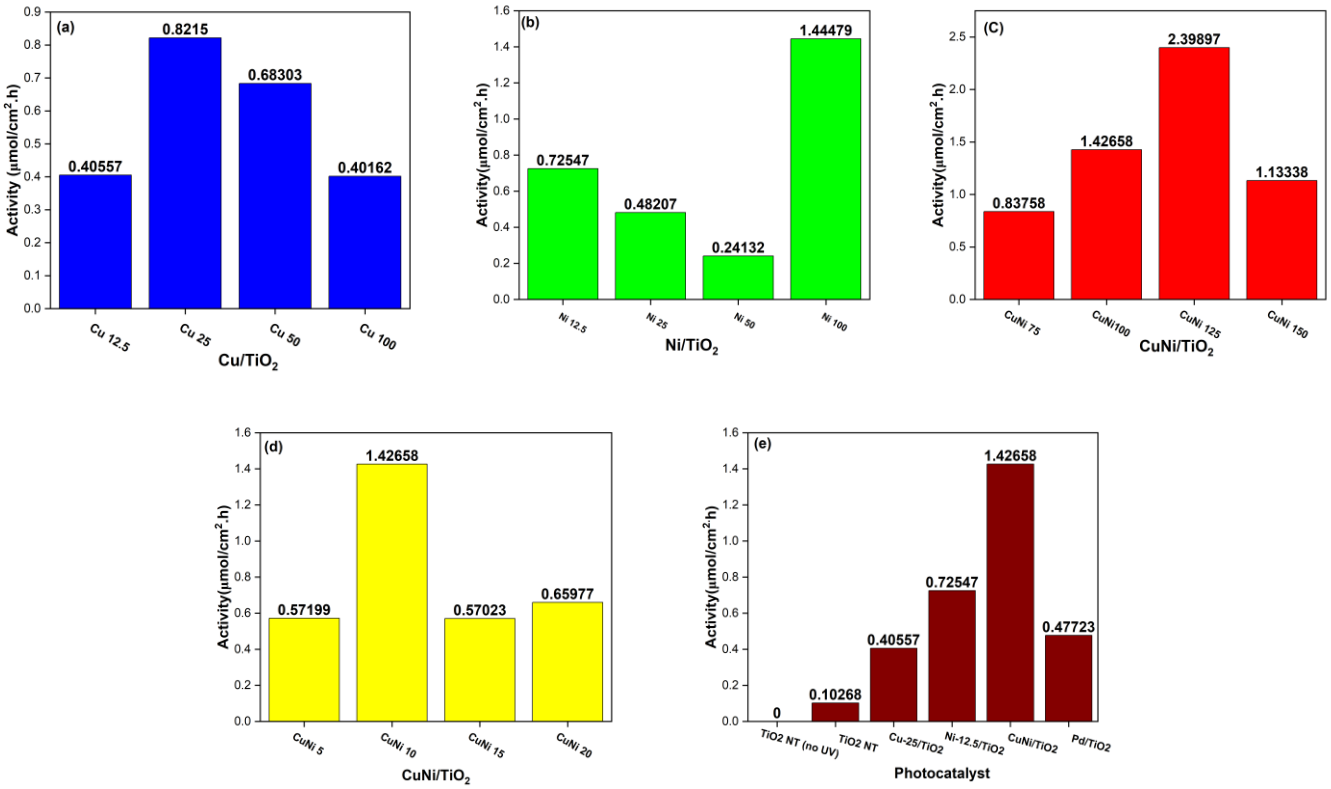

Figure 19: (a) Varying concentrations decoration of Cu/TiO_2 (b) activity of varying concentrations of Ni/TiO_2 photocatalyst. (c) optimizing varying deposition temperatures (d) optimizing varying deposition time (e) overall activity of photocatalysts used

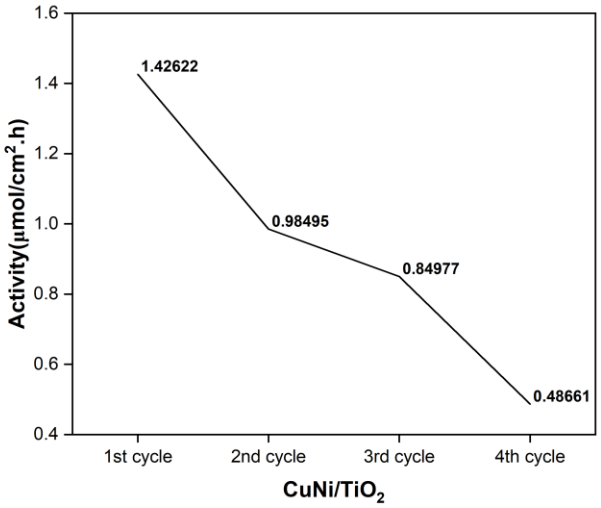

Figure 20: Stability test of $CuNi/TiO_2$

3.3 Conclusion

The best photocatalyst obtained after systematic optimization of concentration, time, and concentration was CuNi. This photocatalyst harnessed the synergistic effect of Ni's electron trapping ability and improved Cu's light absorption. However, the issue of stability after 16 hours needs further investigation. It was discovered that the photocatalyst was operating at an efficiency of ~35% after four cycles (16 hours). To solve this stability problem, annealing the photocatalyst under an inert atmosphere or exploring other metal alloys in binary or ternary forms would be examined. Overall, best concentration, time, temperature, and loading were investigated to obtain a $CuNi/ TiO_2$ photocatalyst with an improved activity ~14 times that of the bare TiO_2 nanotube using green and sustainable principles. This research paves the way for the cost-effective synthesis of photocatalysts, demonstrating the potential of environmentally friendly principles such as limited solvent and energy usage.

Microwave-assisted decoration of Cu and Ni on TiO_2 nanotube photocatalyst achieved a significant and uniform deposition of the photocatalyst. However, the challenge of this method is the possible localized overheating and scalability issues. Building upon this, in the subsequent chapter (Chapter 4), LA -RAM, a novel mechanochemical process that uses acoustic frequency is was used in the loading of Cu and Ni on TiO_2 powders using just 500µL of solvent (water). This process's rapid and intense mixing leads to the homogenous mixing of the TiO_2 with the metal precursors. Unlike microwave decoration, this technique is favorable for scale-up because reaction conditions used in the laboratory scale need no re-optimization when scaling up to larger batches. The objective of this project is not just to produce an effective photocatalyst considering the catalytic performance but also the scalability and practicality of each synthesis technique.

CHAPTER 4: SCALABLE AND GREEN SYNTHESIS OF Cu-Ni/TiO_2 FOR HYDROGEN PRODUCTION USING LA-RAM

4.1 Introduction

The use of pestle and mortar to induce chemical reactions is an agelong practice often referred to as grindstone chemistry. There is no detailed account of how this process first came to light. However, Theophratus, in a short booklet dubbed "On stones," first reported the reduction of cinnabar to mercury by grinding in a copper mortar with a copper pestle in 315 BC [108-109]. This process is easy to operate in most laboratory settings because no specialized equipment is needed. Nevertheless, it is not practical for long reaction times. Again, the reproducibility of this technique is a significant issue as it is hinged on the operator's physical strength. Since then, much work has been done, and numerous developments have occurred in designing techniques that offer control of input energy, reproducibility, and safety to its operators [110]. William Ostwald first coined the term mechanochemistry in 1891 [111-112]. However, Gerhard Heinkle introduced its accepted definition as the field of chemistry characterized by physical and chemical changes due to the application of mechanical energy in 1984 [112].

The emergence of this field has become promising in addressing the limitations of conventional synthetic processes, which involve heating and the use of expensive hazardous chemicals [112]. Solvents are essential for dispersing, dissolving, or transporting chemicals in a reaction. However, efficient mixing techniques such as ball milling or grinding can offer an alternative and efficient route for the reaction between solid mixtures [113]. Nonetheless, even in solventless mixing or grinding, solvents are essential for separating the reaction product in its pure form. Notably, liquid-assisted grinding with limited amounts of solvent is reported to be more time—and energy-efficient than dry milling [112]. Mechanochemistry has become particularly common in catalysis, where it is used to synthesize supported metal nanoparticles, metal oxide nanoparticles, composite particles, etc.[112], [114-115]Ball milling and twin-screw extrusion methods have often been used [116].

Nascent technologies such as ultrasonic or acoustic frequency sample agitation have recently been explored for cocrystal formation [116]. However, LA-RAM, a ball-free, cleaner, simpler, and easily scalable method, is one emerging promising method that can compete with the existing mechanochemical methods [117-118]. This process uses limited liquid, similar to liquid-assisted grinding, inducing chemical reactions by resonant acoustic mixing. It has succeeded in synthesizing some nanomaterials, such as ZIF-L MOFs, which was impossible with conventional mechanochemical processes [116].

TiO_2 is the most used photocatalyst since its first use by Honda and Fujishima in splitting water[8]. This is due to its nontoxicity, chemical stability, and suitable redox potential for photocatalytic water splitting [80-81].

However, it still has limitations, such as narrow absorption and recombination of charge carriers, due to its wide band gap of around 3.2 eV. Its light absorption has been restricted to the UV region, which comprises only 3-5% of solar radiation [36-37]. Cocatalyst loading is one of the methods explored to address the limitations of recombination and minimal light absorption [11,75]. However, noble metals such as Pt, Pd, Au, etc, are often used and have been found to enhance significantly the activity of TiO_2 when loaded [11,73].

This is due to high work function. Pt is good at trapping electrons due to its high work function to prolong the lifetime of charge carriers [119], [120].

On the other hand, due to the surface plasmon resonant effect, Au has also improved the light absorption of photocatalysts [121]. However, due to their expensive and limited nature, they are not ideal for industrial processes. Hence, low-cost and earth-abundant transition metals have been explored to replace them [10]. Transitional metals such as Ni also have a high work function and can form a Schottky barrier to help restrict the recombination of charge carriers. Copper has also shown excellence in improving the light absorption abilities of photocatalysts [11,13,75]. Several methods have been explored in the loading of photocatalysts. However, conventional methods have limitations due to the extensive use of solvents and are energy-intensive [112]. Hence, efforts have been made to use green and sustainable ways of synthesizing photocatalysts. LA-RAM, a mechanochemical synthesis method, offers promise due to the limited solvent use, minimum energy, and ease of scale[116,117].

In this project, we used different copper loadings to decorate TiO_2 to find the best loading that yields the best activity. Additionally, we explored a mixture of copper and nickel loading on TiO_2 to exploit this mixture's synergistic effects. The decoration process was carried out using Liquid-Assisted Resonant Acoustic Mixing. This study aimed to discover low-cost, scalable, green, and sustainable methods for synthesizing photocatalysts.

4.2 Experimental section

4.2.1 Materials

Titanium (IV) oxide, 98+%, anatase powder(Thermo Scientific Chemicals), Copper (II) nitrate trihydrate, 99%, pure(Thermo Scientific Chemicals), Nickel (II) nitrate hexahydrate,98%(Thermo Scientific Chemicals), Sodium borohydride,98%(Thermo Scientific Chemicals), Ascorbic acid, 99% (Thermo Scientific Chemicals), and Triethanolamine,98+%(Thermo Scientific Chemicals).

4.2.2 Loading of Cu and Ni on TiO_2

TiO_2 with a mass of 0.95 mg is weighed. The Cu-TiO_2 has different mass ratios of 0.025, 0.050, and 0.10, and the Cu and Ni mass ratio is 0.025 each on CuNi/TiO_2. These mixtures are labelled as 0.025Cu/TiO_2, 0.050Cu/TiO_2, 0.10 Cu/TiO_2 and 0.025 CuNi/TiO_2.Ascorbic with the same mole ratio as the metal precursors is added to the mixture. Sodium Borohydride is also examined and used in the same mole ratio as the $Cu(NO3)_2.3H_2O$ in the 0.025 Cu/TiO_2 mixture. 500 µL of water is added to each mixture and mixed in the LabRAM II-Resodyn at an acceleration of 95 g for 1hr.

The resulting mixture is washed with water four times in a sonicator to isolate the reaction product from unreacted reactants. It is then dried in an oven at 70°C and left overnight. The dried sample is then ground in a mortar using a pestle to obtain finer particles.

4.2.3 Characterization

The crystal phase and composition of the TiO_2 powder and metals were examined using a benchtop powder X-ray Diffraction (XRD) instrument with a Hypix-400MF 2D hybrid pixel array detector (HPAD) at room temperature. The morphology of the decorated TiO_2 powders with LA RAM and Coprecipitation was studied using a REGULUS 8230 Scanning Electron Microscope.

The surface chemistry of the decorated TiO_2 was observed using Thermo-scientific K-Alpha. Finally, the UV Vis diffuse reflectance spectra were recorded using Carry 5000 UV-Vis NIR from Agilent Technologies, where pure TiO_2 powder was used as the baseline. The photocatalyst was examined at room temperature from a 250-800 nm wavelength.

4.2.4 Photocatalytic test

20 mg of photocatalyst was weighed and transferred into a quartz reactor, along with 9 mL of distilled water and 1 mL of TEOA. The reaction was then purged with nitrogen for 30 minutes to remove any interfering oxygen. The reaction occurred in an enclosed box with a customized LED cell of UV (placed on a magnetic stir plate. After 4 hours, the HER was analyzed using a Clarus 590 gas chromatograph.

4.3 Results and Discussion

First, the photocatalyst's morphology was studied using a Phenom ProX Scanning Electron Microscope (SEM) with EDS capability. The mixture particles in the co-precipitation method were individual, ordered, and smaller(Fig. 21c). However, the particles in the LARAM were less ordered and formed agglomerates (Fig. 21a & b)

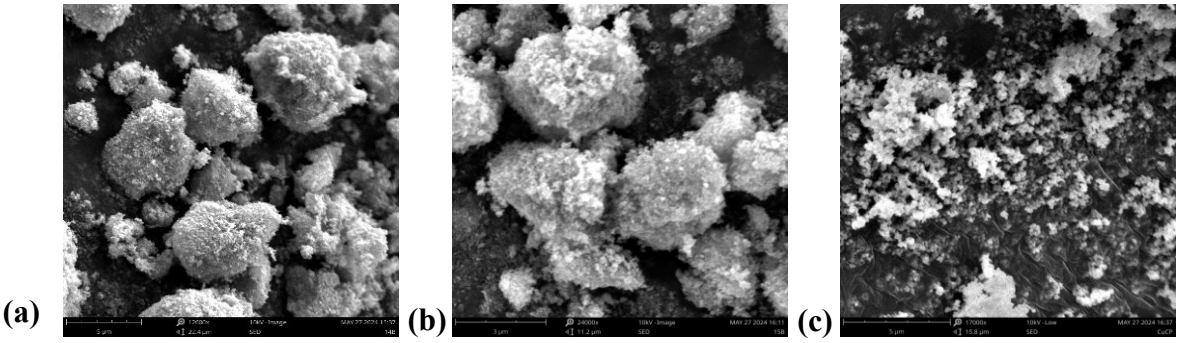

Figure 21: SEM images of (a) 0.025 Cu/TiO_2 (LA-RAM),(b) 0.025 $CuNi/TiO_2$ (LA-RAM), and (c) 0.050 Cu/TiO_2 (co-precipitation)

Furthermore, XRD analysis was used to analyze any defects or phase changes in the mixture using XRD. The anatase and rutile phase of TiO_2 was still seen at ~25.3° and 27.4° respectively which corresponds to the characteristic peak for anatase and rutile [122]. However, the intensity of the peak decreased significantly in the LA-RAM synthesized composites, and there were rutile peaks detected; this could be a result of the local heating and high pressure due to the acoustic mixing, which initiated the phase transition [123,124]. Peaks for Cu_2O were seen on the XRD spectra for 0.025 Cu/TiO_2 (Fig. 22). There was Cu_2O(111) signals and signals detected on 0.025$CuNi/TiO_2$(Fig. 22). However, the XRD spectra for the co-precipitation synthesized 0.050 Cu/TiO_2 showed signals for CuO (111) and phase (Fig. 22).

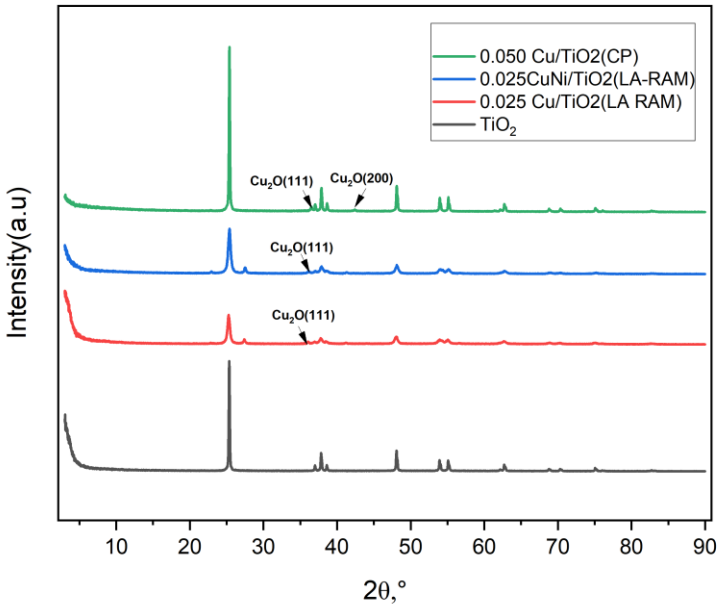

Figure 22: XRD spectra of 0.025Cu/TiO_2(LA-RAM), 0.025 CuNi/TiO_2(LA-RAM), 0.050 Cu/TiO_2 (cp) and TiO_2

Moreover, SEM-EDS was used to analyze the dispersion of the copper and nickel particles on the TiO_2. The copper and nickel particles were not evenly distributed on the surface of TiO_2 but were detected at various points on the surface of TiO_2. The weight percentage of Cu in the 0.025 Cu/TiO_2 was 0.96 wt%. 0.025 CuNi/TiO_2 also had a weight percentage of 0.89 wt% for Cu and 0.22 wt% for Ni. The amount of copper detected in the coprecipitation synthesized 0.050 Cu/TiO_2 was 4.10 wt% for Cu. This also further confirms the presence of copper and nickel in the TiO_2 mixture, confirming that the decoration was successful but not evenly distributed in both the LA-RAM and coprecipitation methods.

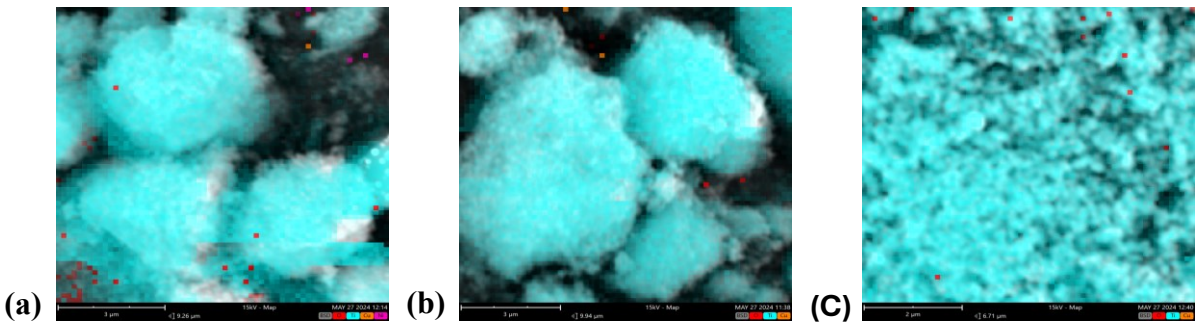

Figure 23: EDS of (a) 0.025 Cu /TiO_2 ,(b) 0.025 CuNi/TiO_2 and (c) 0.050 Cu/TiO_2

In addition, XPS analysis was done using thermoscientific K-Alpha to determine the mixtures' chemical state and surface composition. The XPS analysis was done for the most active photocatalysts: 0.025 Cu/TiO_2 and 0.025 $CuNi/TiO_2$.

For, 0.025 Cu/TiO_2, there was a peak detected at 933.4eV(Fig. 24c) which corresponds to CuO [96], [97]. Again, the peak for Ti was the same at ~459.7eV(fig a), and oxygen also had its characteristic peak at 530.5eV[125], [126]. However, there was a signal at ~531eV, which corresponds to the hydroxyl group(OH) (fig b). This can result from the small amount of water added or the free water molecule in the precursor [95].

On the other hand, for 0.025 $CuNi/TiO_2$, a characteristic CuO peak at 933.4eV was also detected. However, there was no extra oxygen peak besides the characteristic one at 530.6eV. Ti also showed its characteristic signal at 459.4 eV [125], [126]. This shows no change in the chemical state of the titanium and oxygen. No nickel signal was detected by the XRD. This can be due to XPS's sensitivity to surface composition only, whereas XRD detects bulk composition [127], [128].

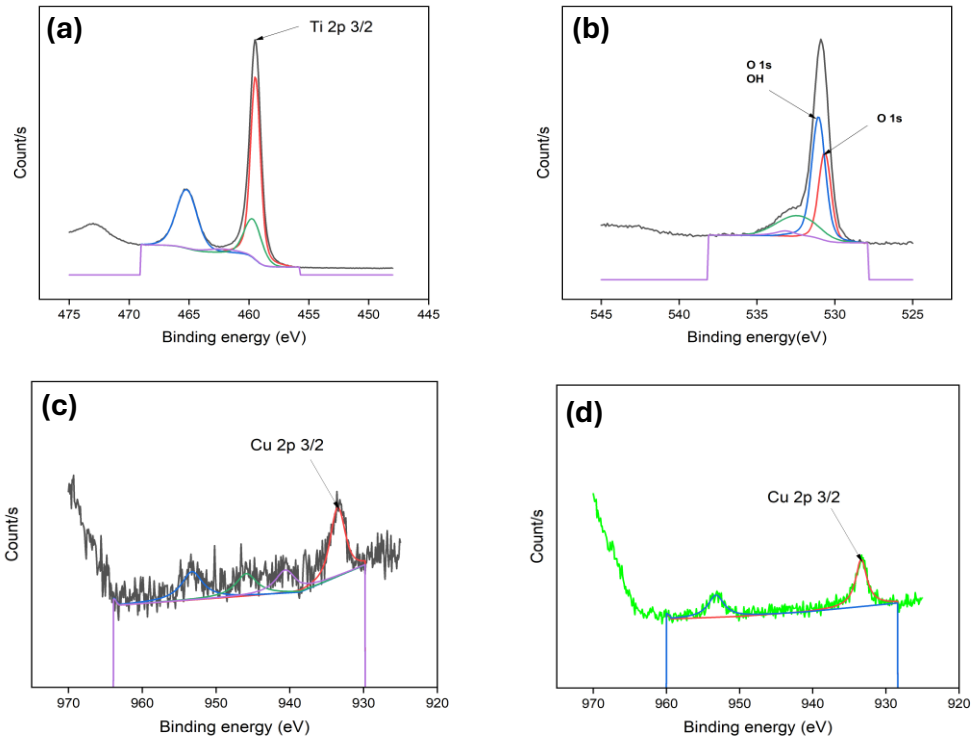

Figure 24: XPS of (a) Ti in TiO_2 ,(b) o in 0.025 Cu/TiO_2 ,(c) Cu in Cu/TiO_2 and (d) 0.025$CuNi/TiO_2$

Furthermore, the optical properties of the photocatalyst were studied for the most active photocatalysts synthesized by LA-RAM and the conventional coprecipitation method to investigate their ability to light-harnessing abilities. The spectra region was from 200-800 nm.

There is a characteristic peak around 385 nm, which corresponds to the TiO_2 band gap energy of 3.2 eV [129]. The LA RAM synthesized composites had improved light absorption compared to the one synthesized by Coprecipitation. There was improved light absorption from around 450-800 nm, with a characteristic peak of copper or copper-containing compounds around 600 nm due to the effect of surface plasmon resonance [102]. Again, the improved visible light absorption can be explained by the narrow band gap of CuO (1.8eV) [104].

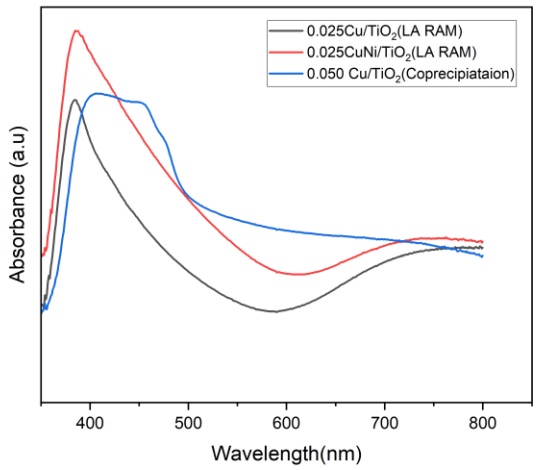

Figure 25: UV-VIS diffuse reflectance of the most active photocatalysts in LA-RAM compared to that synthesized by coprecipitation.

Finally, the photocatalytic assessment was performed to investigate the activity and the loading that yielded the best activity in Cu/TiO_2. Again, $CuNi/TiO_2$ was also analyzed to study the synergistic effect of copper and nickel loadings using this method, as was done earlier via microwave decoration. This assessment was done in both UV and visible light. Firstly, the reaction was done in the dark to ensure only light initiated this process. The water and TEOA were irradiated to light for 4 hours to make sure the photocatalyst solely initiated the hydrogen produced.

The 0.025 Cu/TiO_2 catalyst was the most active in the UV region (Fig. 25a). This might result from achieving uniform loading, which leads to enhanced activity. Also, it could be seen from the graph that synthesized photocatalysts exhibited an enhanced activity of several magnitudes compared to the bare TiO_2. This confirms the effective loading of copper on TiO_2 by the LA-RAM. Studies show a synergistic effect between rutile and anatase, which leads to enhanced activity. This could also partly account for this improved activity [130], [131].

Again, the 0.050 Cu/TiO_2 (SB) using Sodium borohydride as a reducing agent showed significantly enhanced activity compared to ascorbic acid. This could be because sodium borohydride has a better-reducing potential than ascorbic acid. However, in visible light, they exhibited similar activity. Hence, more data would be needed to justify this.

0.025 $CuNi/TiO_2$, on the other hand, showed higher activity than 0.050 Cu/TiO_2, as seen in Fig (25a). This enhanced activity, as shown by 0.025 $CuNi/TiO_2$, results from the synergistic effect between copper and nickel in enhanced light absorption and electron trapping, respectively.

In the same way, $CuNi/TiO_2$ was the most active for visible light(Fig. 25b). This is due to copper's improved light absorption in the visible region due to the surface plasmon effect and nickel's electron trapping abilities. Additionally, 0.025 Cu/TiO_2 also showed improved activity, indicating that it had the optimum loading of copper.

Notably, despite being less active in the UV region, the coprecipitation synthesized photocatalyst $0.050Cu/TiO_2$(CP) showed a slight increase in activity than the bare TiO_2 in the visible light. This could be due to the shielding of most of the TiO_2 surface since it is the part that absorbs UV. This is further evidenced by identifying an ideal loading of ~0.96 wt% for $0.025Cu/TiO_2$ to yield an enhanced activity. However, from the SEM-EDS, the loading of Cu in 0.050 Cu/TiO_2 from Coprecipitation was 4.10 wt%. This excessive loading might cause reduced activity even lower than bare TiO_2 in the UV region.

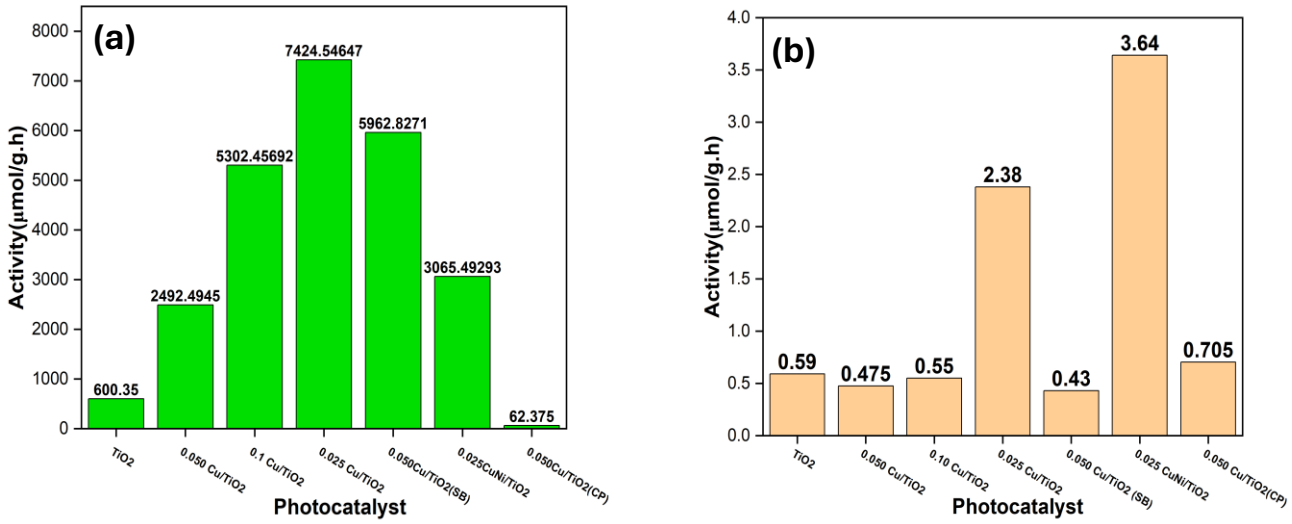

Figure 26: Photocatalytic H_2 generation of various samples under (a) uv light and (b) visible light

4.4 Conclusion

In summary, photocatalysts with UV and visible light activity, specifically 0.025 Cu/TiO_2 and 0.025CuNi, were synthesized using liquid-assisted Resonance Acoustic Mixing, a novel method for synthesizing photocatalysts. The UV-active photocatalyst showed significant activity of 7424.5467 μmol/g·h, approximately 12 times the activity of bare TiO_2. The 0.025 CuNi, which was most active in the visible region, also demonstrated a substantial increase in visible light activity of 3.64 μmol/g·h, about 6 times that of TiO_2 alone. The enhanced activity is attributed to the synergistic effect of Cu's light harvesting and Ni's electron trapping abilities. Additionally, the introduction of the rutile phase by the process led to mixed phases, likely triggered by local heating. This synergistic effect between the anatase phase and the rutile phase is reported to contribute to improved photocatalytic activity. Overall, the research successfully explored the use of liquid-assisted resonant acoustic mixing to produce an efficient and cost-effective photocatalyst using environmentally friendly principles.

CHAPTER 5: CONCLUSION AND OUTLOOK

To sum it up, this study investigated the synthesis of cost-effective photocatalysts that were UV and visible active using environmentally friendly principles.

Initially, microwave deposition was used to decorate TiO_2 nanotubes with Cu and Ni. The individual activity of Cu and Ni were studied initially. The resulting best Cu and Ni were then combined and loaded on a TiO_2 nanotube to form $CuNi/TiO_2$. $CuNi/TiO_2$ exhibited the highest activity of about 12 times that of the bare TiO_2 nanotube. However, after 4 consecutive cycle runs, it exhibited just 35% of its initial activity. This instability highlights the need for further study either by annealing in a reduced atmosphere like H_2 or forming alternative metal mixtures.

To build on this, a novel process in photocatalyst synthesis, LA-RAM, was also explored in the synthesis of $CuNi/TiO_2$. Cu's varying loadings were examined before mixing it with Ni to examine the synergistic effect between Ni's electron trapping ability and Cu's improved light absorption.

0.025 Cu/TiO_2 was found to be the most active in the UV region, while $CuNi/TiO_2$ exhibited an enhanced visible light absorption about 6 times that of the bare TiO_2. Again, it was discovered that the mixed phase of TiO_2 after LA-RAM decoration, which might be due to induced local heating, also has been reported to exhibit a synergistic effect, which helps preserve the lifetime of charge carriers.

To conclude, this research lays a solid foundation for developing cost-effective and efficient photocatalysts using environmentally friendly methods: microwave-assisted and LA-RAM methods. Significant improvements in photocatalytic activity were achieved through careful optimization of concentration, time, temperature, and metal loading. Future efforts will prioritize enhancing the stability of these materials and exploring alternative material systems to translate these findings into practical, durable solutions not only for renewable energy applications but also for environmental remediation.

REFERENCES

[1] P. K. Ramanujam, B. Parameswaran, B. Bharathiraja, and A. Magesh, Eds., *Bioenergy: Impacts on Environment and Economy*. in Energy, Environment, and Sustainability. Singapore: Springer Nature Singapore, 2023. doi: 10.1007/978-981-99-3002-9.

[2] I. Karakurt and G. Aydin, "Development of regression models to forecast the CO2 emissions from fossil fuels in the BRICS and MINT countries," *Energy*, vol. 263, p. 125650, Jan. 2023, doi: 10.1016/j.energy.2022.125650.

[3] M. R. Shaner, S. J. Davis, N. S. Lewis, and K. Caldeira, "Geophysical constraints on the reliability of solar and wind power in the United States," *Energy Environ. Sci.*, vol. 11, no. 4, pp. 914–925, 2018, doi: 10.1039/C7EE03029K.

[4] S. Atilhan, S. Park, M. M. El-Halwagi, M. Atilhan, M. Moore, and R. B. Nielsen, "Green hydrogen as an alternative fuel for the shipping industry," *Curr. Opin. Chem. Eng.*, vol. 31, p. 100668, Mar. 2021, doi: 10.1016/j.coche.2020.100668.

[5] "Hydrogen explained - U.S. Energy Information Administration (EIA)." [Online]. Available: https://www.eia.gov/energyexplained/hydrogen/

[6] H. Song, S. Luo, H. Huang, B. Deng, and J. Ye, "Solar-Driven Hydrogen Production: Recent Advances, Challenges, and Future Perspectives," *ACS Energy Lett.*, vol. 7, no. 3, pp. 1043–1065, Mar. 2022, doi: 10.1021/acsenergylett.1c02591.

[7] J. C. Colmenares, R. Luque, J. M. Campelo, F. Colmenares, Z. Karpiński, and A. A. Romero, "Nanostructured Photocatalysts and Their Applications in the Photocatalytic Transformation of Lignocellulosic Biomass: An Overview," *Materials*, vol. 2, no. 4, pp. 2228–2258, Dec. 2009, doi: 10.3390/ma2042228.

[8] A. Fujishima and K. Honda, "Electrochemical Photolysis of Water at a Semiconductor Electrode," *Nature*, vol. 238, no. 5358, pp. 37–38, Jul. 1972, doi: 10.1038/238037a0.

[9] P. Arunachalam, K. Nagai, M. S. Amer, M. A. Ghanem, R. J. Ramalingam, and A. M. Al-Mayouf, "Recent Developments in the Use of Heterogeneous Semiconductor Photocatalyst Based Materials for a Visible-Light-Induced Water-Splitting System—A Brief Review," *Catalysts*, vol. 11, no. 2, p. 160, Jan. 2021, doi: 10.3390/catal11020160.

[10] J. Ran, J. Zhang, J. Yu, M. Jaroniec, and S. Z. Qiao, "Earth-abundant cocatalysts for semiconductor-based photocatalytic water splitting," *Chem Soc Rev*, vol. 43, no. 22, pp. 7787–7812, 2014, doi: 10.1039/C3CS60425J.

[11] L. Tian, X. Guan, S. Zong, A. Dai, and J. Qu, "Cocatalysts for Photocatalytic Overall Water Splitting: A Mini Review," *Catalysts*, vol. 13, no. 2, p. 355, Feb. 2023, doi: 10.3390/catal13020355.

[12] P. Mondal, A. Sinha, N. Salam, A. S. Roy, N. R. Jana, and S. M. Islam, "Enhanced catalytic performance by copper nanoparticle–graphene based composite," *RSC Adv.*, vol. 3, no. 16, p. 5615, 2013, doi: 10.1039/c3ra23280h.

[13] D. T. Tran, V. H. Hoa, S. Prabhakaran, D. H. Kim, N. H. Kim, and J. H. Lee, "Activated CuNi@Ni Core@shell structures via oxygen and nitrogen dual coordination assembled on 3D CNTs-graphene hybrid for high-performance water splitting," *Appl. Catal. B Environ.*, vol. 294, p. 120263, Oct. 2021, doi: 10.1016/j.apcatb.2021.120263.

[14] M. Younas, S. Shafique, A. Hafeez, F. Javed, and F. Rehman, "An Overview of Hydrogen Production: Current Status, Potential, and Challenges," *Fuel*, vol. 316, p. 123317, May 2022, doi: 10.1016/j.fuel.2022.123317.

[15] R. Kothari, D. Buddhi, and R. L. Sawhney, “Comparison of environmental and economic aspects of various hydrogen production methods,” *Renew. Sustain. Energy Rev.*, vol. 12, no. 2, pp. 553–563, Feb. 2008, doi: 10.1016/j.rser.2006.07.012.
[16] P. J. Megía, A. J. Vizcaíno, J. A. Calles, and A. Carrero, “Hydrogen Production Technologies: From Fossil Fuels toward Renewable Sources. A Mini Review,” *Energy Fuels*, vol. 35, no. 20, pp. 16403–16415, Oct. 2021, doi: 10.1021/acs.energyfuels.1c02501.
[17] M. Ji and J. Wang, “Review and comparison of various hydrogen production methods based on costs and life cycle impact assessment indicators,” *Int. J. Hydrog. Energy*, vol. 46, no. 78, pp. 38612–38635, Nov. 2021, doi: 10.1016/j.ijhydene.2021.09.142.
[18] Z. Abdin, A. Zafaranloo, A. Rafiee, W. Mérida, W. Lipiński, and K. R. Khalilpour, “Hydrogen as an energy vector,” *Renew. Sustain. Energy Rev.*, vol. 120, p. 109620, Mar. 2020, doi: 10.1016/j.rser.2019.109620.
[19] L. Emami Taba, M. F. Irfan, W. A. M. Wan Daud, and M. H. Chakrabarti, “The effect of temperature on various parameters in coal, biomass and CO-gasification: A review,” *Renew. Sustain. Energy Rev.*, vol. 16, no. 8, pp. 5584–5596, Oct. 2012, doi: 10.1016/j.rser.2012.06.015.
[20] K. Stańczyk *et al.*, “Experimental simulation of hard coal underground gasification for hydrogen production,” *Fuel*, vol. 91, no. 1, pp. 40–50, Jan. 2012, doi: 10.1016/j.fuel.2011.08.024.
[21] T. Sutardi, L. Wang, N. Karimi, and M. C. Paul, “Utilization of H_2O and CO_2 in Coal Particle Gasification with an Impact of Temperature and Particle Size,” *Energy Fuels*, vol. 34, no. 10, pp. 12841–12852, Oct. 2020, doi: 10.1021/acs.energyfuels.0c02280.
[22] C. Acar and I. Dincer, “Comparative assessment of hydrogen production methods from renewable and non-renewable sources,” *Int. J. Hydrog. Energy*, vol. 39, no. 1, pp. 1–12, Jan. 2014, doi: 10.1016/j.ijhydene.2013.10.060.
[23] P. Nikolaidis and A. Poullikkas, “A comparative overview of hydrogen production processes,” *Renew. Sustain. Energy Rev.*, vol. 67, pp. 597–611, Jan. 2017, doi: 10.1016/j.rser.2016.09.044.
[24] D. Hariharan *et al.*, “Catalytic partial oxidation reformation of diesel, gasoline, and natural gas for use in low temperature combustion engines,” *Fuel*, vol. 246, pp. 295–307, Jun. 2019, doi: 10.1016/j.fuel.2019.02.003.
[25] R. Ma, B. Xu, and X. Zhang, “Catalytic partial oxidation (CPOX) of natural gas and renewable hydrocarbons/oxygenated hydrocarbons—A review,” *Catal. Today*, vol. 338, pp. 18–30, Nov. 2019, doi: 10.1016/j.cattod.2019.06.025.
[26] P. Arku, B. Regmi, and A. Dutta, “A review of catalytic partial oxidation of fossil fuels and biofuels: Recent advances in catalyst development and kinetic modelling,” *Chem. Eng. Res. Des.*, vol. 136, pp. 385–402, Aug. 2018, doi: 10.1016/j.cherd.2018.05.044.
[27] H. H. Cho, V. Strezov, and T. J. Evans, “A review on global warming potential, challenges and opportunities of renewable hydrogen production technologies,” *Sustain. Mater. Technol.*, vol. 35, p. e00567, Apr. 2023, doi: 10.1016/j.susmat.2023.e00567.
[28] O. Bičáková and P. Straka, “Production of hydrogen from renewable resources and its effectiveness,” *Int. J. Hydrog. Energy*, vol. 37, no. 16, pp. 11563–11578, Aug. 2012, doi: 10.1016/j.ijhydene.2012.05.047.
[29] I. Dincer, “Green methods for hydrogen production,” *Int. J. Hydrog. Energy*, vol. 37, no. 2, pp. 1954–1971, Jan. 2012, doi: 10.1016/j.ijhydene.2011.03.173.

[30] R. Ameta, M. S. Solanki, S. Benjamin, and S. C. Ameta, “Photocatalysis,” in *Advanced Oxidation Processes for Waste Water Treatment*, Elsevier, 2018, pp. 135–175. doi: 10.1016/B978-0-12-810499-6.00006-1.
[31] L. Yuan, C. Han, M.-Q. Yang, and Y.-J. Xu, “Photocatalytic water splitting for solar hydrogen generation: fundamentals and recent advancements,” *Int. Rev. Phys. Chem.*, vol. 35, no. 1, pp. 1–36, Jan. 2016, doi: 10.1080/0144235X.2015.1127027.
[32] A. Kudo and Y. Miseki, “Heterogeneous photocatalyst materials for water splitting,” *Chem Soc Rev*, vol. 38, no. 1, pp. 253–278, 2009, doi: 10.1039/B800489G.
[33] “ChemSusChem - 2009 - Navarro Yerga - Water Splitting on Semiconductor Catalysts under Visible-Light Irradiation.pdf.”
[34] K. Villa, J. R. Galán-Mascarós, N. López, and E. Palomares, “Photocatalytic water splitting: advantages and challenges,” *Sustain. Energy Fuels*, vol. 5, no. 18, pp. 4560–4569, 2021, doi: 10.1039/D1SE00808K.
[35] Q. Xu, L. Zhang, B. Cheng, J. Fan, and J. Yu, “S-Scheme Heterojunction Photocatalyst,” *Chem*, vol. 6, no. 7, pp. 1543–1559, Jul. 2020, doi: 10.1016/j.chempr.2020.06.010.
[36] Y. Wang *et al.*, “Mimicking Natural Photosynthesis: Solar to Renewable H $_2$ Fuel Synthesis by Z-Scheme Water Splitting Systems,” *Chem. Rev.*, vol. 118, no. 10, pp. 5201–5241, May 2018, doi: 10.1021/acs.chemrev.7b00286.
[37] C. Chen, W. Ma, and J. Zhao, “Semiconductor-mediated photodegradation of pollutants under visible-light irradiation,” *Chem. Soc. Rev.*, vol. 39, no. 11, p. 4206, 2010, doi: 10.1039/b921692h.
[38] M. G. Walter *et al.*, “Solar Water Splitting Cells,” *Chem. Rev.*, vol. 110, no. 11, pp. 6446–6473, Nov. 2010, doi: 10.1021/cr1002326.
[39] X. Chen, S. Shen, L. Guo, and S. S. Mao, “Semiconductor-based Photocatalytic Hydrogen Generation,” *Chem. Rev.*, vol. 110, no. 11, pp. 6503–6570, Nov. 2010, doi: 10.1021/cr1001645.
[40] W. Fan, Q. Zhang, and Y. Wang, “Semiconductor-based nanocomposites for photocatalytic H2 production and CO2 conversion,” *Phys. Chem. Chem. Phys.*, vol. 15, no. 8, p. 2632, 2013, doi: 10.1039/c2cp43524a.
[41] S. Shen, L. Zhao, X. Guan, and L. Guo, “Improving visible-light photocatalytic activity for hydrogen evolution over ZnIn2S4: A case study of alkaline-earth metal doping,” *J. Phys. Chem. Solids*, vol. 73, no. 1, pp. 79–83, Jan. 2012, doi: 10.1016/j.jpcs.2011.09.027.
[42] N. Fajrina and M. Tahir, “A critical review in strategies to improve photocatalytic water splitting towards hydrogen production,” *Int. J. Hydrog. Energy*, vol. 44, no. 2, pp. 540–577, Jan. 2019, doi: 10.1016/j.ijhydene.2018.10.200.
[43] S. Bai, J. Jiang, Q. Zhang, and Y. Xiong, “Steering charge kinetics in photocatalysis: intersection of materials syntheses, characterization techniques and theoretical simulations,” *Chem. Soc. Rev.*, vol. 44, no. 10, pp. 2893–2939, 2015, doi: 10.1039/C5CS00064E.
[44] Y. Wang, E. Chen, and J. Tang, “Insight on Reaction Pathways of Photocatalytic CO $_2$ Conversion,” *ACS Catal.*, vol. 12, no. 12, pp. 7300–7316, Jun. 2022, doi: 10.1021/acscatal.2c01012.
[45] T. Teranishi and M. Sakamoto, “Charge Separation in Type-II Semiconductor Heterodimers,” *J. Phys. Chem. Lett.*, vol. 4, no. 17, pp. 2867–2873, Sep. 2013, doi: 10.1021/jz4013504.

[46] I. Bedja and P. V. Kamat, “Capped Semiconductor Colloids. Synthesis and Photoelectrochemical Behavior of TiO 2 -Capped SnO 2 Nanocrystallites,” *J. Phys. Chem.*, vol. 99, no. 22, pp. 9182–9188, Jun. 1995, doi: 10.1021/j100022a035.
[47] N. Serpone, P. Maruthamuthu, P. Pichat, E. Pelizzetti, and H. Hidaka, “Exploiting the interparticle electron transfer process in the photocatalysed oxidation of phenol, 2-chlorophenol and pentachlorophenol: chemical evidence for electron and hole transfer between coupled semiconductors,” *J. Photochem. Photobiol. Chem.*, vol. 85, no. 3, pp. 247–255, Jan. 1995, doi: 10.1016/1010-6030(94)03906-B.
[48] N. Serpone, E. Borgarello, and M. Gratzel, “Visible Light Induced Generation of Hydrogen from HZS in Mixed Semiconductor Dispersions; Improved Efficiency through Inter-particle Electron Transfer”.
[49] A. J. Bard, “Photoelectrochemistry and heterogeneous photo-catalysis at semiconductors,” *J. Photochem.*, vol. 10, no. 1, pp. 59–75, Jan. 1979, doi: 10.1016/0047-2670(79)80037-4.
[50] R. Bala Chandran, S. Breen, Y. Shao, S. Ardo, and A. Z. Weber, “Evaluating particle-suspension reactor designs for Z-scheme solar water splitting *via* transport and kinetic modeling,” *Energy Environ. Sci.*, vol. 11, no. 1, pp. 115–135, 2018, doi: 10.1039/C7EE01360D.
[51] K. Maeda, “Z-Scheme Water Splitting Using Two Different Semiconductor Photocatalysts,” *ACS Catal.*, vol. 3, no. 7, pp. 1486–1503, Jul. 2013, doi: 10.1021/cs4002089.
[52] Q. Xu, L. Zhang, J. Yu, S. Wageh, A. A. Al-Ghamdi, and M. Jaroniec, “Direct Z-scheme photocatalysts: Principles, synthesis, and applications,” *Mater. Today*, vol. 21, no. 10, pp. 1042–1063, Dec. 2018, doi: 10.1016/j.mattod.2018.04.008.
[53] Q. Li *et al.*, “Highly Efficient Visible-Light-Driven Photocatalytic Hydrogen Production of CdS-Cluster-Decorated Graphene Nanosheets,” *J. Am. Chem. Soc.*, vol. 133, no. 28, pp. 10878–10884, Jul. 2011, doi: 10.1021/ja2025454.
[54] E. Borgarello, J. Kiwi, M. Graetzel, E. Pelizzetti, and M. Visca, “Visible light induced water cleavage in colloidal solutions of chromium-doped titanium dioxide particles,” *J. Am. Chem. Soc.*, vol. 104, no. 11, pp. 2996–3002, Jun. 1982, doi: 10.1021/ja00375a010.
[55] E. Borgarello, J. Kiwi, E. Pelizzetti, M. Visca, and M. Grätzel, “Photochemical cleavage of water by photocatalysis,” *Nature*, vol. 289, no. 5794, pp. 158–160, Jan. 1981, doi: 10.1038/289158a0.
[56] H. Yan *et al.*, “Visible-light-driven hydrogen production with extremely high quantum efficiency on Pt–PdS/CdS photocatalyst,” *J. Catal.*, vol. 266, no. 2, pp. 165–168, Sep. 2009, doi: 10.1016/j.jcat.2009.06.024.
[57] X. Zong *et al.*, “Enhancement of Photocatalytic H 2 Evolution on CdS by Loading MoS 2 as Cocatalyst under Visible Light Irradiation,” *J. Am. Chem. Soc.*, vol. 130, no. 23, pp. 7176–7177, Jun. 2008, doi: 10.1021/ja8007825.
[58] W. Fan, Q. Zhang, and Y. Wang, “Semiconductor-based nanocomposites for photocatalytic H2 production and CO2 conversion,” *Phys. Chem. Chem. Phys.*, vol. 15, no. 8, p. 2632, 2013, doi: 10.1039/c2cp43524a.
[59] N. Bao, L. Shen, T. Takata, and K. Domen, “Self-Templated Synthesis of Nanoporous CdS Nanostructures for Highly Efficient Photocatalytic Hydrogen Production under Visible Light,” *Chem. Mater.*, vol. 20, no. 1, pp. 110–117, Jan. 2008, doi: 10.1021/cm7029344.
[60] J. Yu and J. Ran, “Facile preparation and enhanced photocatalytic H2-production activity of Cu(OH)2 cluster modified TiO2,” *Energy Environ. Sci.*, vol. 4, no. 4, p. 1364, 2011, doi: 10.1039/c0ee00729c.

[61] Y.-H. Pai and S.-Y. Fang, “Preparation and characterization of porous Nb2O5 photocatalysts with CuO, NiO and Pt cocatalyst for hydrogen production by light-induced water splitting,” *J. Power Sources*, vol. 230, pp. 321–326, May 2013, doi: 10.1016/j.jpowsour.2012.12.078.
[62] S. W. Seo *et al.*, “Enhanced performance of NaTaO3 using molecular co-catalyst [Mo3S4]4+ for water splitting into H2 and O2,” *Chem. Commun.*, vol. 48, no. 84, p. 10452, 2012, doi: 10.1039/c2cc36216c.
[63] P. V. Kamat, “TiO 2 Nanostructures: Recent Physical Chemistry Advances,” *J. Phys. Chem. C*, vol. 116, no. 22, pp. 11849–11851, Jun. 2012, doi: 10.1021/jp305026h.
[64] A. K. Agegnehu, C.-J. Pan, J. Rick, J.-F. Lee, W.-N. Su, and B.-J. Hwang, “Enhanced hydrogen generation by cocatalytic Ni and NiO nanoparticles loaded on graphene oxide sheets,” *J. Mater. Chem.*, vol. 22, no. 27, p. 13849, 2012, doi: 10.1039/c2jm30474k.
[65] A. Kudo, K. Sayama, A. Tanaka, K. Asakura, K. Maruya, and T. Onishi, “Nickel-Loaded K4Nb60 17 Photocatalyst in the Decomposition of H20 into H2 and O2: Structure and Reaction Mechanism”.
[66] H. Husin *et al.*, “Photocatalytic hydrogen production on nickel-loaded LaxNa1−xTaO3 prepared by hydrogen peroxide-water based process,” *Green Chem.*, vol. 13, no. 7, p. 1745, 2011, doi: 10.1039/c1gc15070g.
[67] X. Wang *et al.*, “Photocatalytic Overall Water Splitting Promoted by an α–β phase Junction on Ga 2 O 3,” *Angew. Chem.*, vol. 124, no. 52, pp. 13266–13269, Dec. 2012, doi: 10.1002/ange.201207554.
[68] H. Aitom, “Photocatalytic Decomposition of Water Vapour on an NO-SrTiO, Catalyst”.
[69] K. Maeda *et al.*, “Photocatalytic Overall Water Splitting Promoted by Two Different Cocatalysts for Hydrogen and Oxygen Evolution under Visible Light,” *Angew. Chem. Int. Ed.*, vol. 49, no. 24, pp. 4096–4099, Jun. 2010, doi: 10.1002/anie.201001259.
[70] N. Sakamoto *et al.*, “Highly dispersed noble-metal/chromia (core/shell) nanoparticles as efficient hydrogen evolution promoters for photocatalytic overall water splitting under visible light,” *Nanoscale*, vol. 1, no. 1, p. 106, 2009, doi: 10.1039/b9nr00186g.
[71] “Advanced Materials - 2016 - Meng - Nanometals for Solar-to-Chemical Energy Conversion From Semiconductor-Based.pdf.”
[72] Z. Zhang, S.-W. Cao, Y. Liao, and C. Xue, “Selective photocatalytic decomposition of formic acid over AuPd nanoparticle-decorated TiO 2 nanofibers toward high-yield hydrogen production,” *Appl. Catal. B Environ.*, vol. 162, pp. 204–209, Jan. 2015, doi: 10.1016/j.apcatb.2014.06.055.
[73] N. Xiao, S. Li, X. Li, L. Ge, Y. Gao, and N. Li, “The roles and mechanism of cocatalysts in photocatalytic water splitting to produce hydrogen,” *Chin. J. Catal.*, vol. 41, no. 4, pp. 642–671, Apr. 2020, doi: 10.1016/S1872-2067(19)63469-8.
[74] P. Zhang, T. Song, T. Wang, and H. Zeng, “In-situ synthesis of Cu nanoparticles hybridized with carbon quantum dots as a broad spectrum photocatalyst for improvement of photocatalytic H2 evolution,” *Appl. Catal. B Environ.*, vol. 206, pp. 328–335, Jun. 2017, doi: 10.1016/j.apcatb.2017.01.051.
[75] “Small Structures - 2022 - Zhao - Transition-Metal-Based Cocatalysts for Photocatalytic Water Splitting (1).pdf.”
[76] D. E. Naugle, Ed., *Energy development and wildlife conservation in western North America*. Washington, DC: Island Press, 2011.

[77] F. Dufuor, *The Costs and Implications of Our Demand for Energy: A Comparative and Comprehensive Analysis of the Available Energy Resources: How Fossil Fuels Have Created an Energy Crisis/Exploring Our Alternatives/The Future of Energy*. 2018.
[78] N. F. Gray, *Facing Up to Global Warming: What is Going on and How You Can Make a Difference?* Cham: Springer International Publishing, 2015. doi: 10.1007/978-3-319-20146-7.
[79] Mitch Jacoby, "Commercializing low-cost solar cells," *CEN Glob. Enterp.*, vol. 94, no. 18, pp. 30–35, May 2016, doi: 10.1021/cen-09418-cover.
[80] J. Schneider *et al.*, "Understanding TiO $_2$ Photocatalysis: Mechanisms and Materials," *Chem. Rev.*, vol. 114, no. 19, pp. 9919–9986, Oct. 2014, doi: 10.1021/cr5001892.
[81] J. Zhang, B. Tian, L. Wang, M. Xing, and J. Lei, *Photocatalysis: Fundamentals, Materials and Applications*, vol. 100. in Lecture Notes in Chemistry, vol. 100. Singapore: Springer Singapore, 2018. doi: 10.1007/978-981-13-2113-9.
[82] Y. Li *et al.*, "A template/electrochemical deposition method for fabricating silver nanorod arrays based on porous anodic alumina," *Nanomater. Nanotechnol.*, vol. 7, p. 184798041771754, Jan. 2017, doi: 10.1177/1847980417717543.
[83] "Advanced Science - 2016 - Ge - One-dimensional TiO2 Nanotube Photocatalysts for Solar Water Splitting (1).pdf."
[84] Z. Su and W. Zhou, "Formation, morphology control and applications of anodic TiO2 nanotube arrays," *J. Mater. Chem.*, vol. 21, no. 25, p. 8955, 2011, doi: 10.1039/c0jm04587j.
[85] V. Zwilling, M. Aucouturier, and E. Darque-Ceretti, "Anodic oxidation of titanium and TA6V alloy in chromic media. An electrochemical approach," *Electrochimica Acta*, vol. 45, no. 6, pp. 921–929, Dec. 1999, doi: 10.1016/S0013-4686(99)00283-2.
[86] D. Gong *et al.*, "Titanium oxide nanotube arrays prepared by anodic oxidation," *J. Mater. Res.*, vol. 16, no. 12, pp. 3331–3334, Dec. 2001, doi: 10.1557/JMR.2001.0457.
[87] E. Gabano and M. Ravera, "Microwave-Assisted Synthesis: Can Transition Metal Complexes Take Advantage of This 'Green' Method?," *Molecules*, vol. 27, no. 13, p. 4249, Jun. 2022, doi: 10.3390/molecules27134249.
[88] T. Theivasanthi and M. Alagar, "Titanium dioxide".
[89] Md. Ashraful Alam, R. Kumar Bishwas, S. Mostofa, and S. Akter Jahan, "Low-temperature synthesis and crystal growth behavior of nanocrystal anatase-TiO2," *Mater. Lett.*, vol. 354, p. 135396, Jan. 2024, doi: 10.1016/j.matlet.2023.135396.
[90] D. O. Scanlon *et al.*, "Band alignment of rutile and anatase TiO2," *Nat. Mater.*, vol. 12, no. 9, pp. 798–801, Sep. 2013, doi: 10.1038/nmat3697.
[91] S.-C. Li and U. Diebold, "Reactivity of TiO $_2$ Rutile and Anatase Surfaces toward Nitroaromatics," *J. Am. Chem. Soc.*, vol. 132, no. 1, pp. 64–66, Jan. 2010, doi: 10.1021/ja907865t.
[92] K. K. M., N. G., V. K. V., S. V. B., S. B., and V. A., "Improved H2 yields over Cu-Ni-TiO2 under solar light irradiation: Behaviour of alloy nano particles on photocatalytic H2O splitting," *Appl. Catal. B Environ.*, vol. 299, p. 120654, Dec. 2021, doi: 10.1016/j.apcatb.2021.120654.
[93] "Chemistry A European J - 2013 - Gao - Nickel Hydroxide Nanoparticle Activated Semi-metallic TiO2 Nanotube Arrays for (1).pdf."
[94] W. Wang, S. Liu, L. Nie, B. Cheng, and J. Yu, "Enhanced photocatalytic H $_2$ -production activity of TiO $_2$ using Ni(NO $_3$) $_2$ as an additive," *Phys Chem Chem Phys*, vol. 15, no. 29, pp. 12033–12039, 2013, doi: 10.1039/C2CP43628K.

[95] “Advanced Materials - 2016 - Ke - Surface-Charge-Mediated Formation of H-TiO2 Ni OH 2 Heterostructures for High-Performance (1).pdf.”
[96] N. S. McIntyre and M. G. Cook, “X-ray photoelectron studies on some oxides and hydroxides of cobalt, nickel, and copper,” *Anal. Chem.*, vol. 47, no. 13, pp. 2208–2213, Nov. 1975, doi: 10.1021/ac60363a034.
[97] I. G. Casella and M. Gatta, “Anodic electrodeposition of copper oxide/hydroxide films by alkaline solutions containing cuprous cyanide ions,” *J. Electroanal. Chem.*, vol. 494, no. 1, pp. 12–20, Dec. 2000, doi: 10.1016/S0022-0728(00)00375-2.
[98] L. G. Devi, “Enhanced photocatalytic activity of transition metal ions Mn2+, Ni2+ and Zn2+ doped polycrystalline titania for the degradation of Aniline Blue under UV/solar light,” 2010.
[99] “Chemistry An Asian Journal - 2016 - Cha - Free-Standing Membranes to Study the Optical Properties of Anodic TiO2 Nanotube.pdf.”
[100] “Wang et al. - 2013 - Enhanced photocatalytic H 2 -production.pdf.”
[101] C. Lin *et al.*, “Plasmon-induced broad spectrum photocatalytic overall water splitting: Through non-noble bimetal nanoparticles hybrid with reduced graphene oxide,” *Colloids Surf. Physicochem. Eng. Asp.*, vol. 646, p. 128962, Aug. 2022, doi: 10.1016/j.colsurfa.2022.128962.
[102] K. Grochowska *et al.*, “Laser induced formation of copper species over TiO2 nanotubes towards enhanced water splitting performance,” *Int. J. Hydrog. Energy*, vol. 45, no. 38, pp. 19192–19205, Jul. 2020, doi: 10.1016/j.ijhydene.2020.05.054.
[103] C. Lin *et al.*, “Plasmon-induced broad spectrum photocatalytic overall water splitting: Through non-noble bimetal nanoparticles hybrid with reduced graphene oxide,” *Colloids Surf. Physicochem. Eng. Asp.*, vol. 646, p. 128962, Aug. 2022, doi: 10.1016/j.colsurfa.2022.128962.
[104] D. S. D. Lima, J. C. Cruz, V. A. Luciano, M. A. Nascimento, A. P. C. Teixeira, and R. P. Lopes, “Enhanced photocatalytic activity of cobalt-doped titanate nanotube heterostructures decorated with Cu2O-CuO nanoparticles for organic pollutant degradation under UV and visible irradiation,” *Appl. Surf. Sci.*, vol. 563, p. 150313, Oct. 2021, doi: 10.1016/j.apsusc.2021.150313.
[105] A. Cots, P. Bonete, and R. Gómez, “Improving the Stability and Efficiency of CuO Photocathodes for Solar Hydrogen Production through Modification with Iron,” *ACS Appl. Mater. Interfaces*, vol. 10, no. 31, pp. 26348–26356, Aug. 2018, doi: 10.1021/acsami.8b09892.
[106] H. Xing, L. E, Z. Guo, D. Zhao, and Z. Liu, “Enhancement in the charge transport and photocorrosion stability of CuO photocathode: The synergistic effect of spatially separated dual-cocatalysts and p-n heterojunction,” *Chem. Eng. J.*, vol. 394, p. 124907, Aug. 2020, doi: 10.1016/j.cej.2020.124907.
[107] H. Xing, L. E, Z. Guo, D. Zhao, X. Li, and Z. Liu, “Exposing the photocorrosion mechanism and control strategies of a CuO photocathode,” *Inorg. Chem. Front.*, vol. 6, no. 9, pp. 2488–2499, 2019, doi: 10.1039/C9QI00780F.
[108] L. Takacs, “The historical development of mechanochemistry,” *Chem. Soc. Rev.*, vol. 42, no. 18, p. 7649, 2013, doi: 10.1039/c2cs35442j.
[109] L. Takacs, “Quicksilver from cinnabar: The first documented mechanochemical reaction?,” *JOM*, vol. 52, no. 1, pp. 12–13, Jan. 2000, doi: 10.1007/s11837-000-0106-0.
[110] M. Leonardi, M. Villacampa, and J. C. Menéndez, “Multicomponent mechanochemical synthesis,” *Chem. Sci.*, vol. 9, no. 8, pp. 2042–2064, 2018, doi: 10.1039/C7SC05370C.

[111] V. V. Boldyrev and K. Tkacˇova, “Mechanochemistry of Solids: Past, Present, and Prospects”.
[112] C. Xu, S. De, A. M. Balu, M. Ojeda, and R. Luque, “Mechanochemical synthesis of advanced nanomaterials for catalytic applications,” *Chem. Commun.*, vol. 51, no. 31, pp. 6698–6713, 2015, doi: 10.1039/C4CC09876E.
[113] “Adv Synth Catal - 2007 - Rodríguez - Solvent-Free Carbon-Carbon Bond Formations in Ball Mills.pdf.”
[114] U. Kamolphop *et al.*, “Low-Temperature Selective Catalytic Reduction (SCR) of NO_x with *n* -Octane Using Solvent-Free Mechanochemically Prepared Ag/Al_2O_3 Catalysts,” *ACS Catal.*, vol. 1, no. 10, pp. 1257–1262, Oct. 2011, doi: 10.1021/cs200326m.
[115] A. R. Siamaki, Y. Lin, K. Woodberry, J. W. Connell, and B. F. Gupton, “Palladium nanoparticles supported on carbon nanotubes from solventless preparations: versatile catalysts for ligand-free Suzuki cross coupling reactions,” *J. Mater. Chem. A*, vol. 1, no. 41, p. 12909, 2013, doi: 10.1039/c3ta12512b.
[116] H. M. Titi, J.-L. Do, A. J. Howarth, K. Nagapudi, and T. Friščić, “Simple, scalable mechanosynthesis of metal–organic frameworks using liquid-assisted resonant acoustic mixing (LA-RAM),” *Chem. Sci.*, vol. 11, no. 29, pp. 7578–7584, 2020, doi: 10.1039/D0SC00333F.
[117] A. A. L. Michalchuk, K. S. Hope, S. R. Kennedy, M. V. Blanco, E. V. Boldyreva, and C. R. Pulham, “Ball-free mechanochemistry: *in situ* real-time monitoring of pharmaceutical co-crystal formation by resonant acoustic mixing,” *Chem. Commun.*, vol. 54, no. 32, pp. 4033–4036, 2018, doi: 10.1039/C8CC02187B.
[118] A. Vandenberg and K. Wille, “Evaluation of resonance acoustic mixing technology using ultra high performance concrete,” *Constr. Build. Mater.*, vol. 164, pp. 716–730, Mar. 2018, doi: 10.1016/j.conbuildmat.2017.12.217.
[119] “Liu et al. - 2020 - Positively charged Pt-based cocatalysts an orient.pdf.”
[120] H. Cai *et al.*, “Bridging effect of Co heteroatom between g-C3N4 and Pt NPs for enhanced photocatalytic hydrogen evolution,” *Chem. Eng. J.*, vol. 394, p. 124964, Aug. 2020, doi: 10.1016/j.cej.2020.124964.
[121] Z. Zhang, Z. Wang, S.-W. Cao, and C. Xue, “Au/Pt Nanoparticle-Decorated TiO_2 Nanofibers with Plasmon-Enhanced Photocatalytic Activities for Solar-to-Fuel Conversion,” *J. Phys. Chem. C*, vol. 117, no. 49, pp. 25939–25947, Dec. 2013, doi: 10.1021/jp409311x.
[122] V. Collins-Martínez, A. López Ortiz, and A. Aguilar Elguézabal, “Influence of the Anatase/Rutile Ratio on the TiO2 Photocatalytic Activity for the Photodegradation of Light Hydrocarbons,” *Int. J. Chem. React. Eng.*, vol. 5, no. 1, Nov. 2007, doi: 10.2202/1542-6580.1613.
[123] P. Xiaoyan, C. Yi, M. Xueming, and Z. Lihui, “Phase Transformation of Nanocrystalline Anatase Powders Induced by Mechanical Activation,” *J. Am. Ceram. Soc.*, vol. 87, no. 6, pp. 1164–1166, Jun. 2004, doi: 10.1111/j.1551-2916.2004.01164.x.
[124] A. Gajović, K. Furić, N. Tomašić, S. Popović, Ž. Skoko, and S. Musić, “Mechanochemical preparation of nanocrystalline TiO2 powders and their behavior at high temperatures,” *J. Alloys Compd.*, vol. 398, no. 1–2, pp. 188–199, Aug. 2005, doi: 10.1016/j.jallcom.2005.02.004.
[125] L. D. Than *et al.*, “Highly Visible Light Activity of Nitrogen Doped TiO2 Prepared by Sol–Gel Approach,” *J. Electron. Mater.*, vol. 46, no. 1, pp. 158–166, Jan. 2017, doi: 10.1007/s11664-016-4894-6.

[126] X. Xu, W. Zhang, Y. Li, P. Wang, and Y. Zhang, “Synthesis of Co3O4@TiO2 catalysts for oxygen evolution and oxygen reduction reactions,” *Microporous Mesoporous Mater.*, vol. 335, p. 111844, Apr. 2022, doi: 10.1016/j.micromeso.2022.111844.
[127] M. A. Peck and M. A. Langell, “Comparison of Nanoscaled and Bulk NiO Structural and Environmental Characteristics by XRD, XAFS, and XPS,” *Chem. Mater.*, vol. 24, no. 23, pp. 4483–4490, Dec. 2012, doi: 10.1021/cm300739y.
[128] M. K. Rahman, F. Nemouchi, T. Chevolleau, P. Gergaud, and K. Yckache, “Ni and Ti silicide oxidation for CMOS applications investigated by XRD, XPS and FPP,” *Mater. Sci. Semicond. Process.*, vol. 71, pp. 470–476, Nov. 2017, doi: 10.1016/j.mssp.2017.06.025.
[129] F. Tanos *et al.*, “Graphene oxide-induced CuO reduction in TiO2/CaTiO3/Cu2O/Cu composites for photocatalytic degradation of drugs via peroxymonosulfate activation,” *Appl. Surf. Sci.*, vol. 656, p. 159698, May 2024, doi: 10.1016/j.apsusc.2024.159698.
[130] F. J. Al-Maliki, O. A. Hammadi, and E. A. Al-Oubidy, “Optimization of Rutile/Anatase Ratio in Titanium Dioxide Nanostructures prepared by DC Magnetron Sputtering Technique,” *Iraqi J. Sci.*, 2019.
[131] Y. Wei, M. V. Tokina, A. V. Benderskii, Z. Zhou, R. Long, and O. V. Prezhdo, “Quantum dynamics origin of high photocatalytic activity of mixed-phase anatase/rutile TiO2,” *J. Chem. Phys.*, vol. 153, no. 4, p. 044706, Jul. 2020, doi: 10.1063/5.0014179.